

Cryogenic Materials Characterization and Thermal Contact Optimization

By

Jared Valois

A thesis submitted in partial fulfillment of the requirements for the degree of:

Master of Science

(Mechanical Engineering)

at the

University of Wisconsin-Madison

2024

Graduate Student: Jared Valois

Campus ID: 9077473776

Title: Cryogenic Materials Characterization and Thermal Contact Optimization

Approved by:

Professor Gregory Nellis

Department of Mechanical Engineering

Signature: _____ Date: _____

Professor John Pfothenhauer

Department of Mechanical Engineering

Signature: _____ Date: _____

Abstract

The design of technology that operates at cryogenic temperatures requires an extensive knowledge of the behavior of the materials comprising the design. This work utilized a test facility that allows for the precise measurement of material properties at these cryogenic temperatures. The material of interest was Oxygen Free High Conductivity (OFHC) copper as it is a very common material choice for designs at these temperatures. The two material properties that were investigated and characterized were thermal bulk conductivity and thermal contact resistance. The purpose of these tests was to investigate some of the primary and secondary factors that affect these material properties that have been under-represented in the literature. The thermal bulk conductivity testing focused on the impact that the source of purchase had on the overall conductivity of the sample; samples purchased from different commercial vendors undergo different amounts of work hardening due to differences in manufacturing practices and the level of work hardening directly effects conductivity. The thermal contact resistance testing focused on the impact of contact interface pressure of gold-plated samples. An additional component of this contact resistance testing was investigating the effect of mating and de-mating cycles across this pressure range. The results from this material characterization were then inserted into a newly created thermal simulation framework. The thermal simulation framework was utilized to design and thermally optimize a common component found in these cryogenic technologies, a bolted joint. The successful optimization of this joint indicates that the process of material property characterization followed by the use of this thermal analysis framework could be used to aid in the design of additional cryogenic technologies in the future.

Acknowledgements

Looking back at these two years, I realized that the decision to go to graduate school changed the trajectory of my life for the better. Yes, the classes and research work will impact my future, but it was the relationships with others that really changed my life. And because of this, I have many people to thank.

I would like to thank my advisors Greg Nellis and John Pfothenhauer. Your continued support and confidence have allowed me to grow immensely as both a person and a researcher. In the beginning I remember asking both of you a million dumb questions, and now even if I ask you a bunch of dumb questions it is not quite a million. I cannot thank you enough for your continued effort and the continued patience you have given me these past two years. I couldn't have done it without you.

I would like to thank Kelsey McCusker, Avi Friedman, and Corey Misenheimer from Northrop Grumman. The combined expertise and guidance from this group has helped keep this project moving forward and has helped make it a continued success. I would also like to thank Northrop Grumman for funding this research.

I would like to thank all of the SEL graduate students. The sense of community here has really made work a place that I look forward to being at, which I think says a lot about everyone in this group. Thank you for all of the memories and friendships, these are the things that I will never forget.

I would like to thank Roman Morse for introducing me to this world of research. Your passion and excitement were contagious and was a driving factor in my decision to start down this path. I have and will continue to adopt your motto of 'And Now Let's do Cool Science'.

I would like to thank my family. You were the support system that I could always count on. From venting about my struggles and failures to getting to share my successes you were always there to listen and provide help, even if it was way over the top (cough cough, mom). I could never thank you enough for everything that you do, you really do make my life a great one.

Table of Contents

Abstract.....	ii
Acknowledgements.....	iii
Table of Contents	iv
List of Figures.....	viii
List of Tables.....	x
1 Introduction.....	1
1.1 Motivation.....	1
1.2 Current Contributions	1
2 Test Facility and Equipment.....	3
2.1 Initial Test Facility Design.....	3
2.1.1 Cooling Device.....	3
2.1.2 Chamber Design.....	4
2.1.3 Measurement Instrumentation.....	10
2.2 Test Facility Upgrades	12
2.2.1 Temperature Sensor Calibration.....	12
2.2.2 Control System.....	14
3 Thermal Bulk Conductivity	15
3.1 Literature Review.....	15
3.1.1 Measurement Techniques.....	15
3.1.2 Comparison of Thermal Bulk Conductivity.....	18
3.2 Test Methodology	18

3.2.1	Test Fixture.....	18
3.2.2	Data Collection Procedure	20
3.3	Calculations and Uncertainty Analysis	22
3.3.1	Thermal Bulk Conductivity Total Uncertainty.....	22
3.3.2	Temperature Sensor Uncertainty.....	23
3.3.3	Applied Heat Uncertainty.....	24
3.3.4	Length and Cross-Sectional Area Measurement Uncertainty	26
3.4	Results and Discussion	27
3.4.1	Comparison with Literature	29
3.4.2	RRR Determination.....	30
3.5	Conclusions.....	33
4	Thermal Contact Resistance of Pressed Contacts	35
4.1	Literature Review.....	35
4.1.1	Factors that impact thermal contact resistance.....	36
4.1.2	Models for thermal contact resistance.....	38
4.1.3	Measurement techniques	40
4.2	Test Methodology	42
4.2.1	Test Fixture.....	42
4.2.2	Sample Preparation	45
4.2.3	Data Collection Procedure	47
4.3	Calculations and Uncertainty Analysis	50

4.3.1	Thermal Contact Resistance Total Uncertainty.....	52
4.3.2	Temperature Sensor Uncertainty.....	53
4.3.3	Temperature Drop Through Bulk Material Uncertainty.....	55
4.3.4	Constriction Resistance.....	57
4.3.5	Applied Heat Uncertainty.....	57
4.3.6	Heat Flow Through Fixture Uncertainty.....	59
4.3.7	Length and Cross-Sectional Area Measurement Uncertainty.....	59
4.4	Results and Discussion.....	61
4.5	Conclusions.....	66
5	The Thermal Optimization of a Bolted Joint.....	67
5.1	Literature Review.....	67
5.1.1	Physically Measuring Thermal Contact Resistance.....	67
5.1.2	Using Models to Determine Thermal Contact Resistance.....	68
5.2	Model Construction.....	70
5.3	Simulation Design.....	71
5.4	Results and Discussion.....	74
5.5	Conclusion.....	79
6	Conclusion.....	80
7	References.....	82
	Appendix A: Thermal Bulk Conductivity Procedure & Data Processing.....	85
	Appendix B: Thermal Contact Resistance Procedure & Data Processing.....	98

Appendix C: Test Facility ‘Wiring’ Diagrams 101

List of Figures

Figure 2-1. Cryocooler mounted with the cold heads facing upward inside the vacuum chamber.....	4
Figure 2-2. Vacuum chamber exterior.....	5
Figure 2-3. Thermal jackets mounted on cryocooler platforms.....	6
Figure 2-4. Bolt pattern of second stage platform.....	7
Figure 2-5. Thermal oscillations on the second stage platform.....	8
Figure 2-6. Schematic of the liquid helium dampening pot system.....	9
Figure 2-7. Final liquid helium pot configuration.....	10
Figure 2-8. Instrumentation wiring diagram.....	11
Figure 2-9. Knife-edge clamps.....	12
Figure 2-10. Copper plate mounting surface used for temperature sensor calibration.....	13
Figure 3-1. A test facility that is used to perform comparative thermal bulk conductivity measurements.	16
Figure 3-2. A test facility that is used to perform absolute thermal bulk conductivity measurements.	17
Figure 3-3. Thermal bulk conductivity test fixture.....	19
Figure 3-4. Thermal validation of test fixture design. Image A – Left. Image B – Right.....	20
Figure 3-5. Thermal bulk conductivity results for samples sourced from Sequoia Brass & Copper.....	28
Figure 3-6. Thermal bulk conductivity results for samples sourced from McMaster-Carr.....	28
Figure 3-7. Thermal bulk conductivity results for samples sourced for Thyssen-Krupp.....	29
Figure 3-8. Comparison of measured data with known RRR curves from NIST [13].....	30
Figure 3-9. RRR value at each data point compared to the sample's average RRR value for McMaster-Carr sample 1.....	33
Figure 4-1. Relationship between apparent and real contact area [15].	35
Figure 4-2. A pressed thermal contact resistance test fixture [21]. The letters in the figure correspond to key features; in this case, the three letters of importance are letters C, F, and G which correspond to the heater, linearly mounted temperature sensors, and heat sink respectively.....	42
Figure 4-3. Thermal contact resistance test fixture design.....	43

Figure 4-4. Surface profile along the diameter of the contact interface.....	46
Figure 4-5. Contact interface pressure reading.	46
Figure 4-6. Test fixture for fixture resistance determination.	47
Figure 4-7. Resistance network of the thermal contact resistance test.....	50
Figure 4-8. Contact interface temperature extrapolation.	51
Figure 4-9. De-mate and re-mate thermal contact resistance results.	61
Figure 4-10. Thermal contact resistance results.....	62
Figure 4-11. Thermal contact resistance data as a function of pressure. Determined from the function fit to the collected data.....	64
Figure 4-12. Comparison of measured data and literature data.	65
Figure 5-1. Illustration of the experimental setup for the bolted joint. 1-Heater, 2-Top Plate, 3-bolts, 4-Bottom plate, 5-Cold base plate.....	68
Figure 5-2. General geometry used in the simulations.	70
Figure 5-3. Simulation used to determine the portion of resistance caused by the bulk material.....	72
Figure 5-4. Simulation used to determine the portion of resistance due to contact area reduction.	73
Figure 5-5. Simulation used to determine the portion of resistance due to thermal contact resistance.	73
Figure 5-6. Bolt Configurations. a) – single bolt. b) – two bolt horizontal. c) – two bolt diagonal. d)– four bolt.	75
Figure 5-7. Single bolt results.....	76
Figure 5-8. Two bolt horizontal results.....	76
Figure 5-9. Two bolt diagonal results.	77
Figure 5-10. Four bolt results.....	77
Figure 5-11. Total resistance of the joint as a function of the percentage of the contact area taken up by the bolt.	78

List of Tables

Table 2-1. The three main types of cryogenic cooling devices and their characteristics [2].	3
Table 2-2. Instrumentation for experimental test setup.....	10
Table 2-3. Measurement interval recommendations from Lake Shore Cryotronics.	13
Table 3-1. Constants used in the function developed by The National Bureau of Standards.	31
Table 3-2. Sample average and vendor average RRR values.....	31
Table 4-1. Spring information.	44
Table 4-2. Data used to determine an average effective L/A value.....	49
Table 4-3. Germanium sensor coefficients for uncertainty equations.....	54
Table 4-4. Recalibration uncertainty values.....	54
Table 4-5. Constants for the A-D constant curve fit equations.	63
Table 4-6. Contributing sources of uncertainty.	64
Table 4-7. Comparison of material and surface conditions.....	65
Table 5-1. Contact interface dimensions.....	70
Table 5-2. Geometry component dimensions.....	71

1 Introduction

1.1 Motivation

With the emergence of technologies with operational temperature ranges at or near liquid helium temperatures - a few examples being detector technologies for space applications, ground-based astrophysics experiments studying dark matter, electronic packaging of superconducting circuits, quantum computing technology, or other cryogen-free systems that are conductively cooled by closed-cycle cryocoolers – the understanding of the thermal response of the materials that are used in these systems is critical for effective thermal design.

This need resulted in the creation of a multi-year project spanning multiple graduate student researchers focused on this task specifically. The first phase of the project was completed by the initial graduate student researcher, Kacie Salmon, who designed and validated a test facility that allowed the measure of material properties over a wide range of cryogenic temperatures. The current work is the second phase of the project which consists of using this test facility to begin to perform material property tests and creating a simulation framework that can be used to help make informed thermal design decisions. Future graduate student researchers will expand this work through the investigation of additional materials and test parameters.

The result of this work will be the creation of a large database of material properties that can be implemented into thermal simulations both at the component level and at an overall system level. The end goal is to eventually remove the need to physically test components or systems in order to understand their thermal performance.

1.2 Current Contributions

This work focused on expanding our understanding of the thermal properties of a specific material commonly found at these temperatures, Oxygen Free High Conductivity (OFHC) copper. Due to its frequency of use in cryogenic systems, the material properties of OFHC copper have been investigated

previously, however there is still much to be discovered. The focus of these tests was to investigate the factors that affect these material properties that are under-investigated in the literature.

The two material properties that were investigated were thermal bulk conductivity and thermal contact resistance. Thermal bulk conductivity tests were performed on samples sourced from a variety of different commercial vendors to investigate the variability of conductivity between vendors, likely due to differences in work-hardening. The goal was to make an overall recommendation of the conductivity of OFHC copper regardless of its source. Thermal contact resistance tests focused on the impact of contact interface pressure of gold-plated samples; testing was accomplished both with and without any mate/demate cycles in order to understand the impact of the mate/demate process.

A simulation framework was developed that aimed to identify the different sources of thermal resistance within a component or system. Through this framework, optimization was performed that minimized the sources of resistance that were large. The simulations performed in this work focused on optimizing the bolt configuration of a bolted joint for the given set of material and surface conditions that match the physical tests performed.

2 Test Facility and Equipment

This chapter was broken up into two main sections. The first section summarizes the initial test facility design which was completed by former UW-Madison graduate student, Kacie Salmon. Please refer to her thesis [1] for a more comprehensive review. The second section summarizes the test facility upgrades made for the purposes of the current research objectives.

2.1 Initial Test Facility Design

2.1.1 Cooling Device

When designing a cryogenic test facility, the first decision made was choosing the cooling device. There are many different cooling devices, which can be seen in Table 2-1, and each device has unique characteristics and therefore has optimal uses. It was important that the chosen device would work well with both thermal bulk conductivity and thermal contact resistance measurements.

Table 2-1. The three main types of cryogenic cooling devices and their characteristics [2].

	Immersion Cryostats	Liquid – Flow Cryostats	Cryocoolers
Requires the Availability of Cryogenic Liquid	Yes	Yes	No
Cost	Low	Low	High
Cooling Power	High	Low	Low
Sample Current Handling	High and Low	Low	Low
Vibrations	None	None	Varying Levels
Operating Convenience	Low	Low	High
Sample Cycle Time	Low	Low	High

Using the information contained in the table above, it was determined that a cryocooler was the best fit for these experiments. There are many different commercially available cryocoolers, but for this test facility a Gifford-McMahon Cryocooler was chosen, specifically, an RDK-415D Sumitomo Cryocooler. The cryocooler was connected to a Sumitomo 70L Compressor which provides power and the high-pressure helium. The cold heads of the cryocooler can provide a heat lift of 45 watts at the first stage which sits at

50 K and 1.5 watts at the second stage when at 4.2 K [3]. In addition, the Gifford-McMahon Cryocooler was mounted with the cold heads facing upward to allow for straightforward sample mounting. This can be seen in Figure 2-1.



Figure 2-1. Cryocooler mounted with the cold heads facing upward inside the vacuum chamber.

2.1.2 Chamber Design

The bell jar was constructed from 304 stainless-steel with a 30-inch inner diameter and a height of approximately 30 inches which can be seen in Figure 2-2. The base of the bell jar contains several openings compatible with KF-40 flanges and were used to connect exterior equipment to the interior of the chamber. Two of the openings were used as electrical feedthroughs, one for heater wiring and the other for temperature sensor wiring. An additional two openings were used to connect the vacuum pump and pressure gauge. The remaining openings were not in use and were sealed with blank KF-40 flanges or ConFlats.



Figure 2-2. Vacuum chamber exterior.

Platforms were designed to be attached to both the first and second stage cold heads of the cryocooler. Indium gaskets were inserted at this interface to reduce the thermal contact resistance which in turn reduced the temperature seen at the platform surface. To reduce the radiative heat load from the external environment, thermal jackets manufactured from 6061 aluminum and covered with multi-layer insulation (MLI) were mounted to each of these platforms which can be seen in Figure 2-3. The concentric jackets help with thermal isolation by reducing the temperature difference between each stage and its warmer surroundings. Minimizing the external heat load was important as it was an element of uncertainty in the system which impacts the minimum test temperature set by the heat lift constraint of the cryocooler.

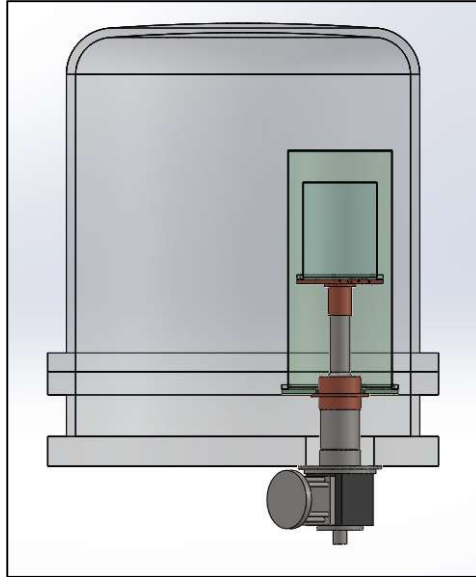


Figure 2-3. Thermal jackets mounted on cryocooler platforms.

The first stage platform was manufactured out of 6061 aluminum. Two openings in the platform were incorporated to allow heater and temperature sensor wiring to be fed through. The wiring was wound around the core of copper bobbins, mounted to the platform interface, to create a thermal sink at this 50-kelvin condition.

The second stage platform consists of a more complex design as it was the location where the test fixtures were mounted. A linear bolt hole pattern was chosen for the platform to allow flexibility in both the design and mounting of the test fixtures. This linear bolt hole pattern can be seen in Figure 2-4. Inserted in each of the bolt holes were stainless steel Heli-Coil inserts which allow direct mounting to the platform. Similar to the first stage platform, copper bobbins were mounted on the platform to thermally sink wire leads to the temperature of the platform. The platform was manufactured out of copper 110 instead of aluminum to have increased thermal conductivity resulting in a reduced temperature at the platform surface. Because of this material change, the difference in thermal contraction between the platform and jacket needed to be considered. It was found that the material stress caused by the difference in contraction could be handled with the bolt stress.

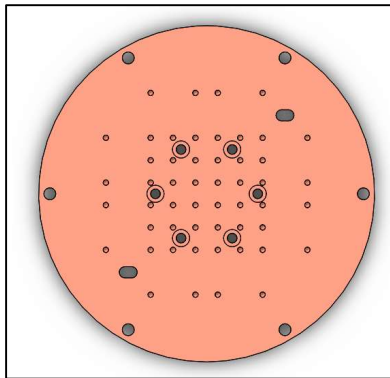


Figure 2-4. Bolt pattern of second stage platform.

When the test facility was constructed, there were large thermal oscillations that occurred at the second stage cold head. These oscillations were an unavoidable consequence of the thermodynamic cycle of Gifford-McMahon Cryocoolers and introduced a source of uncertainty in the steady state data due to the transient conduction effect. The oscillations varied in magnitude with temperature, but it was observed to be around 0.2 kelvin peak-to-peak at a frequency of 1HZ for a stage temperature of roughly 3.5 kelvin, which can be seen in Figure 2-5.

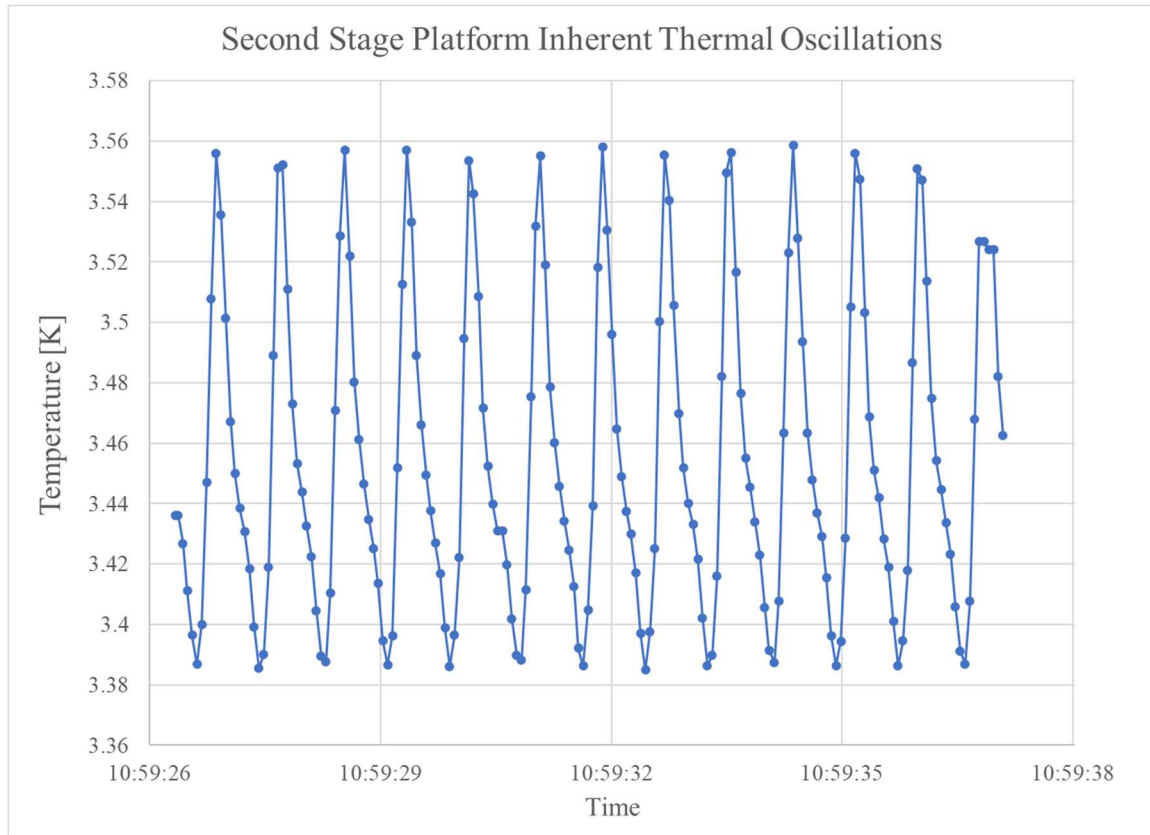


Figure 2-5. Thermal oscillations on the second stage platform.

Oscillations greater than 0.1 kelvin had a significant impact on the uncertainty of thermal bulk conductivity and thermal contact resistance measurements. Therefore, a couple of strategies were implemented to reduce the impact. The first method was to collect a larger number of data points over a period equivalent to an N-number of oscillation cycles and average the results. This results in a more accurate measurement as the fluctuation of the temperature due to this oscillation behavior was smoothed and reduced to the average value of the data measured. The second method performed was the addition of a liquid helium dampening pot. The liquid helium dampening pot sat within the second stage and acted as a thermal mass which reduced the oscillations. Liquid helium was chosen due to its high relative heat capacity at the temperature range of interest. Liquid helium dampening pots were available commercially but due to lead time, integration, and cost restrictions, a system was designed and manufactured in-house. The design can be seen in Figure 2-6.

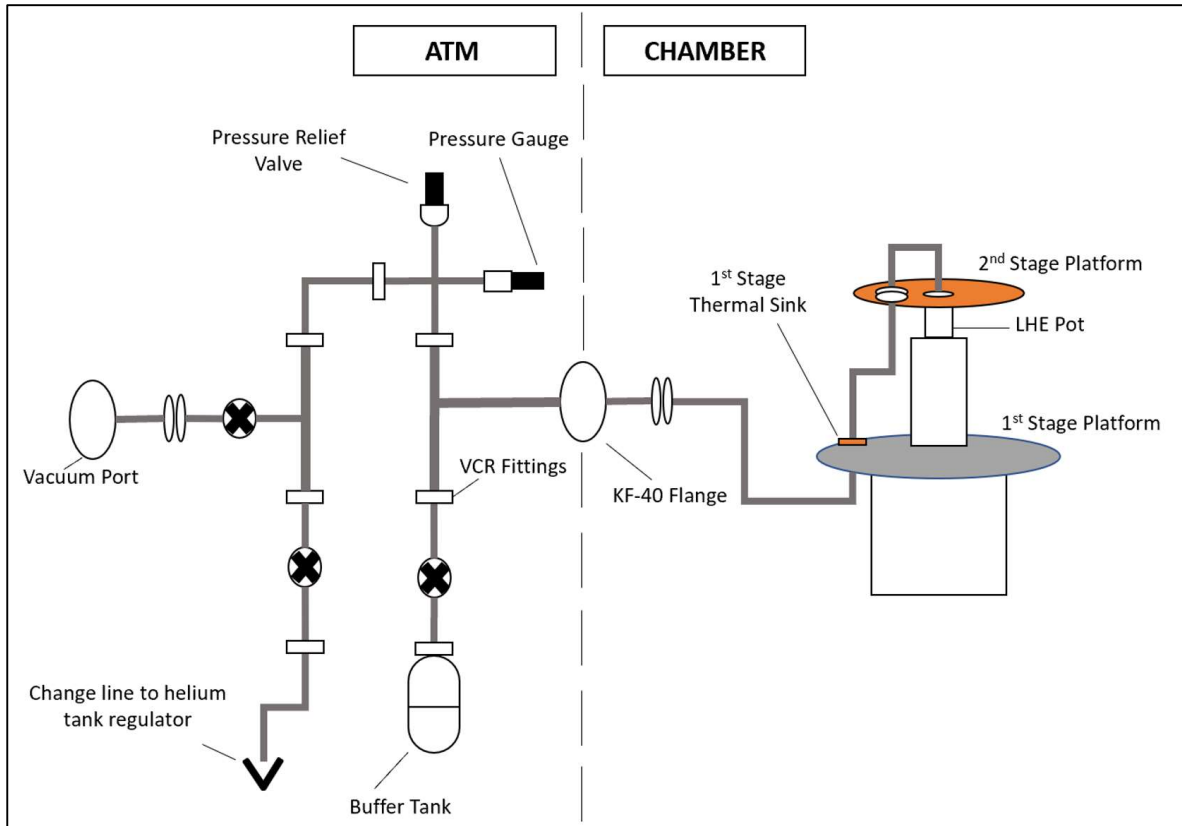


Figure 2-6. Schematic of the liquid helium dampening pot system.

The final configuration had the liquid helium dampening pot in series with the second stage platform. This configuration resulted in the addition of a thermal resistance that raised the no load temperature of the second stage. To eliminate this additional thermal resistance, copper 101 thermal straps were introduced. This final configuration can be seen in Figure 2-7.



Figure 2-7. Final liquid helium pot configuration.

The addition of the liquid helium dampening pot system effectively reduced the oscillations. The peak-to-peak oscillations now measured roughly 0.02 Kelvin, which was deemed acceptable.

2.1.3 Measurement Instrumentation

The instrumentation required to perform thermal bulk conductivity and thermal contact resistance tests included power supplies, multimeters, and a temperature monitor. A list of the instrumentation, including the chosen models is provided in Table 2-2. Figure 2-8 describes the wiring layout going to and from these devices.

Table 2-2. Instrumentation for experimental test setup.

Instrumentation	Function
Granville-Phillips Micro Ion Plus Gauge	Vacuum chamber pressure readings.
Lake Shore 218 Temperature Monitor	Power and read all temperature sensors.
Keithley 2000 Multimeter	Measure main heater voltage.
HP 34401A Multimeter	Measure main heater current (shunt resistor voltage).
BK Precision 1698 DC Power Supply	Power to the main heater.

BK Precision 1685B DC Power Supply	Power to the trim heater.
------------------------------------	---------------------------

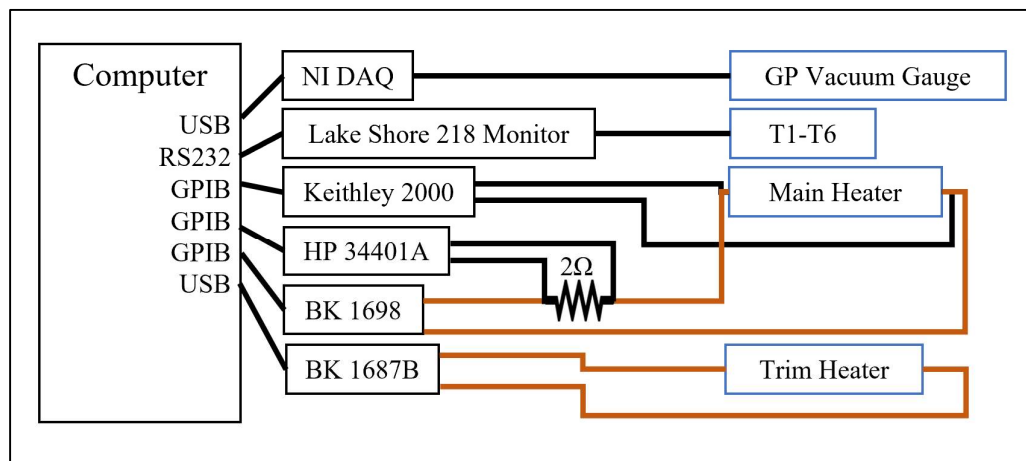


Figure 2-8. Instrumentation wiring diagram.

To clarify, the multimeters were used to measure the main heater power using a four-wire measurement to correctly measure the heater power and not the dissipated heat in the wires that run between the power supply and heater. To determine the heater power, the Keithley 2000 Multimeter measured the voltage across the main heater while the HP 34401A Multimeter indirectly measured the main heater current by measuring the voltage across a high precision 2-ohm shunt resistor in series with the BK Precision 1698 DC Power Supply and main heater.

The test setup utilized two cartridge heaters, one trim heater and one main heater, each with a different function. The main heater was attached to a clam-shell clamp, manufactured out of copper, and mounted directly on the sample near the top of each test fixture, as can be seen in Figure 3-3 and Figure 4-3. This heater was used to apply heat to the sample and was the heating power used in the calculation of thermal bulk conductivity and thermal contact resistance. The trim heater was mounted directly on the second stage platform and acted as a temperature control for the cold head. This temperature control was necessary when taking measurements that occurred at a temperature much higher than the no-load cold head temperature.

The temperature sensors that were used consisted of a combination of Cernox CX-1050-CU-HT-1.4L Sensors and Germanium CR-200A-1000-4D Sensors. The number of temperature sensors in use depended on the test being performed. For thermal bulk conductivity measurements, two sensors were mounted directly on to the sample using knife-edge clamps. The clamp design can be seen in Figure 2-9. For thermal contact resistance measurements, four sensors were mounted directly on the two samples and the remaining two sensors were mounted on the fixture itself.

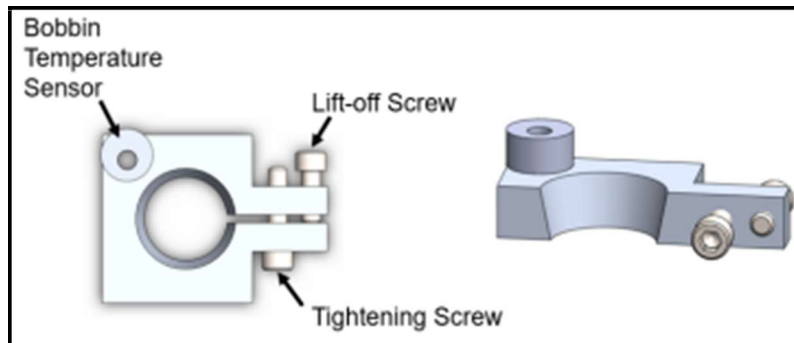


Figure 2-9. Knife-edge clamps.

2.2 Test Facility Upgrades

2.2.1 Temperature Sensor Calibration

Damaged and non-optimally calibrated sensors required a new batch of temperature sensors to be calibrated. For this batch of sensors, the calibration methodology recommended by Lake Shore Cryotronics was followed [4]. A condensed version of this methodology is described below.

An initial calibrated Cernox Temperature Sensor, calibrated over the temperature range of 1.40 - 325 kelvin, was purchased from Lake Shore Cryotronics. The remaining sensors were calibrated against this reference temperature sensor. The first step in the calibration process was to mount the sensors on the second stage cold head as close to one another as possible. This minimized the chance of external factors affecting each sensor differently. This mounting was accomplished by attaching all the sensors to a copper plate which was then bolted to the cold head which can be seen in Figure 2-10. The second step was to take measurements at specific temperature intervals that were recommended by Lake Shore Cryotronics as seen in Table 2-3. For the reference temperature sensor, these measurements included the sensor resistance and

the corresponding temperature. For the sensors undergoing calibration, only sensor resistance was measured. The third step was to correlate the resistance measured by the sensors undergoing calibration to the temperature measured by the reference temperature sensor. The calibration curves for these sensors were in the form of Chebychev Polynomials and were determined using a Matlab Program that was written specifically for this purpose.



Figure 2-10. Copper plate mounting surface used for temperature sensor calibration.

Table 2-3. Measurement interval recommendations from Lake Shore Cryotronics.

Range (K)	Typical number of data points	Interpolation calibration printout interval
0.050 to 0.100	6	0.005
0.100 to 0.300	9	0.010
0.300 to 0.500	5	0.020
0.500 to 1.00	7	0.050
1.00 to 2.00	18	0.10
2.00 to 5.00		0.20
5.00 to 10.0	40	0.50
10.0 to 30.0		1.0
30.0 to 40.0		2.0
40 to 100		5.0
100 to 300	28	5.0
300 to 380		5.0
340 to 480 (silicon diodes)	10	5.0
340 to 480 platinum (400 K upper limit)	15	5.0
480 to 800 platinum sensors only	2	5

Using this methodology, sensors were calibrated with an average uncertainty of 5 millikelvin. This uncertainty was found to be reasonable as the uncertainty was found to be on the same magnitude as the uncertainty coming from other components throughout the system.

2.2.2 Control System

To control all the instrumentation, the program LabVIEW was used. LabVIEW is a graphical programming environment used for instrumentation control, data acquisition, and automation. The LabVIEW program used previously accomplished the first two components, instrumentation control and data acquisition. This was achieved by connecting the instrumentation to the computer via a variety of connection types, as described in Figure 2-8. The program could then be used to control these instruments via user inputs at the LabVIEW interface.

The LabVIEW program has been upgraded and is now able to accomplish all three components, instrumentation control, data acquisition, and automation. Automation was made possible by leveraging the nature of the thermal bulk conductivity and thermal contact resistance tests. For each of these tests, the system reached a quasi-steady state between each measurement. The time it took to reach this steady state was consistent and measurable, allowing for an automation procedure to be written and executed over time. The procedure for a single measurement is as follows:

1. Previous measurement is taken. All data is exported to an excel file under a file name set in a LabVIEW array element.
2. New heating power inputs are read from a previously constructed LabVIEW array element. These inputs are sent to the heater power supplies.
3. The program waits a set amount of time that allows the system to reach a quasi-steady state.
4. The next measurement is taken and the process repeats.

Prior to the use of the upgraded LabVIEW system, both the thermal bulk conductivity and the thermal contact resistance tests took roughly 12 hours to complete and required user inputs roughly every 30 minutes. Using the upgraded system, the test could be started with the push of a single button and ran to completion automatically.

3 Thermal Bulk Conductivity

3.1 Literature Review

Thermal bulk conductivity is a material property that relates the conduction heat flux in a material to a temperature gradient according to Fourier's Law. The experiments performed in this work focused on longitudinal conductivity measurements, which is the conductivity along a significant material length rather than normal to the plane of a thin sheet of material [5].

3.1.1 Measurement Techniques

There are two main steady state measurement techniques that are used to determine thermal bulk conductivity. These techniques are comparative methods and absolute measurements.

The comparative approach is performed by thermally linking the sample of interest in series with samples of two "standard" materials. These materials have had their conductivity determined previously and have values above and below the sample of interest. Heat is then added to the system and the temperature drop across the sample is compared to the temperature drop across each of the two standards. Because these samples are in series and are the same dimensionally, the ratio of the temperature drops is inversely proportional to the ratio of the thermal conductance. Using these ratios, the thermal conductivity of the sample of interest can be determined [6]. An example of a comparative approach test facility can be seen in Figure 3-1.

$$k(\bar{T}) = \frac{LQ}{A\Delta T} \quad 3-1$$

where $k(\bar{T})$ is the temperature dependent thermal conductivity ($\frac{W}{m-K}$) evaluated at the average temperature, L is the axial length between temperature measurements (m), Q is the total heat applied (W), A is the cross-sectional area through which heat flows (m^2), and ΔT is the temperature differential measured (K).

The test facility used to perform this measurement consists of a sample mounted with one end thermally attached to a heat sink, while the other end remains unattached or floating. To this floating end, a resistive heater is mounted to create a temperature gradient through the sample. The power that this heater dissipates is the product of the electrical current flowing through the heater and the voltage drops across it. Temperature sensors are mounted along the axis of the sample to allow a temperature difference to be measured. One example of this type test facility was used by Tuttle et. al. at NASA [5] can be seen in Figure 3-2.

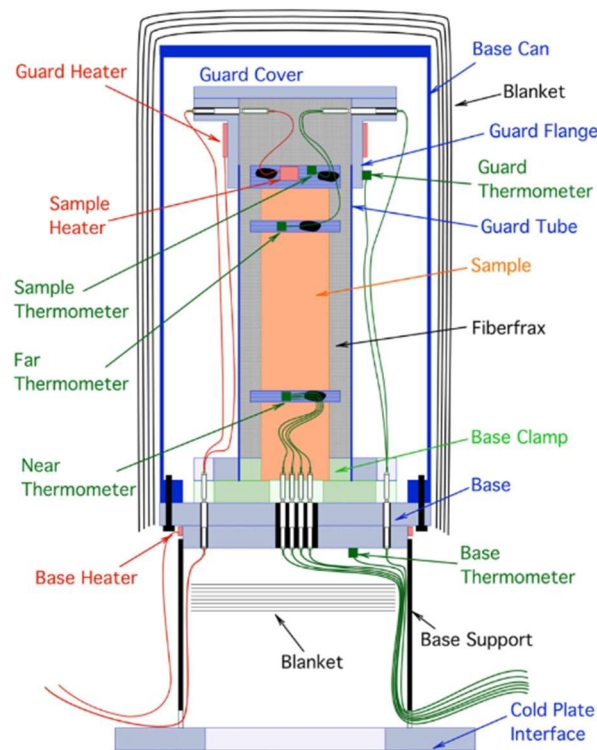


Figure 3-2. A test facility that is used to perform absolute thermal bulk conductivity measurements.

The measurement of thermal bulk conductivity seems straightforward, but, to get highly accurate results, a lot of thought and consideration needs to be put into the design of the test facility to remove or minimize the impact of complications that include ohmic heat generation in the heater leads, radiation between the sample and its environment, the possibility of joint resistances, etc. [5]. There is not a single, ‘correct’ method for addressing each of these issues. In fact, many test facilities resolve these complications using very different techniques.

3.1.2 Comparison of Thermal Bulk Conductivity

Below liquid-nitrogen temperature, the thermal conductivity of relatively pure materials depends strongly on the defect content of the material. Because of this, conductivity varies from sample to sample. The relative purity of a material is quantified using the material’s electrical residual resistance ratio (RRR). RRR is determined using Equation 3-2 [7]:

$$RRR \equiv \frac{\rho_{293K}}{\rho_{4K}} \quad 3-2$$

where RRR is the residual resistance ratio, ρ_{293K} is the materials electrical resistance at room temperature ($\frac{S}{m}$), and ρ_{4K} is the material’s electrical resistance at 4 Kelvin ($\frac{S}{m}$).

3.2 Test Methodology

3.2.1 Test Fixture

The thermal bulk conductivity measurements followed the absolute measurement technique. The test facility was of the same general makeup as that used by Tuttle et. al. at NASA, but a few different design choices were implemented to address the complications inherent to this measurement technique.

The test fixture can be seen in Figure 3-3. It consists of a stainless-steel base that thermally connects the second stage cold plate to the sample. At each of the mounting locations, the cold plate – base and the base – sample, indium foil was used to minimize the resistance at the joints. Mounted on the sample were cylindrical clamps that seat the temperature sensors and resistive heater. For the temperature sensors, knife

edge clamps were utilized to provide a precise temperature measurement location. For the heating element, a standard clamp manufactured out of copper was used to better facilitate heat flow into the sample.

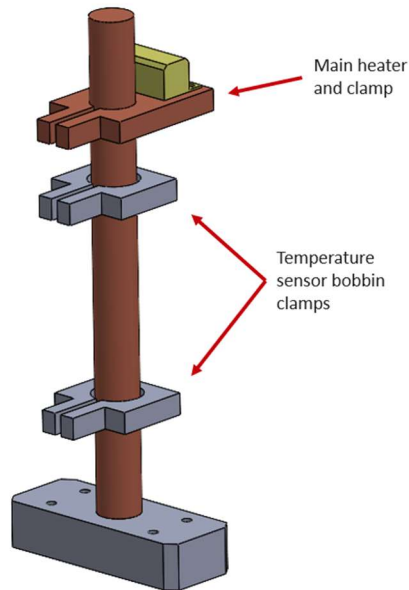


Figure 3-3. Thermal bulk conductivity test fixture.

The use of cylindrical clamps provided three distinct advantages compared to direct mounting on the sample surface. The first advantage was that the use of clamps removes the need for additional machining of the samples after they were purchased. This removes the possibility of adding any work hardening effects that would come with machining the sensor mount locations. The second advantage was the ease of swapping test samples. Instead of demounting and remounting the temperature sensors on every new sample, the cylindrical clamps can be inserted over the free end of the sample and tightened using the tightening screw located on the clamps. The third advantage was that this mounting method does not affect the flow path of the heat. This was confirmed by the previous graduate student researcher, Kacie Salmon, through an ANSYS thermal simulation which can be seen in Figure 3-4. Within Figure 3-4, Image A shows that the temperature distribution becomes isothermal perpendicular to the axis of heat flow above the upper temperature sensor and continues to be isothermal throughout the rest of the sample. This temperature uniformity in the radial direction confirms that the heat flow was unaffected. Image B shows the directional heat flux (moving from right to left). This plot shows that there was little to no temperature gradient across

the knife edge clamps that house the temperature sensors. This was important as it shows that the temperature at the location where the clamp contacts the sample was the same as the temperature at the physical sensor location.

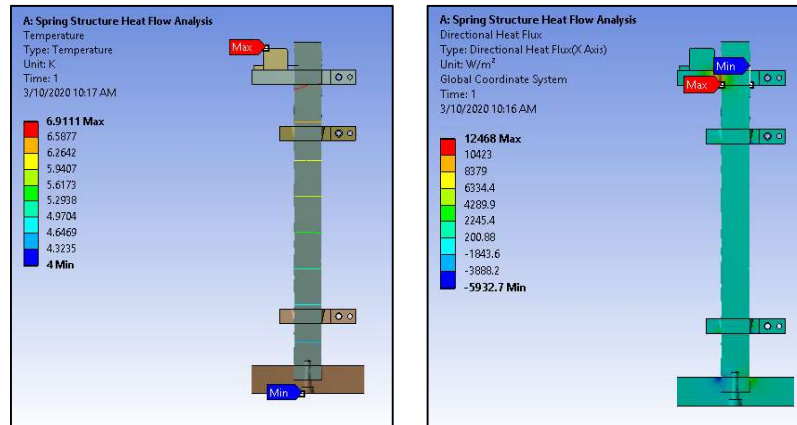


Figure 3-4. Thermal validation of test fixture design. Image A – Left. Image B – Right.

Another consideration with this test facility was how to deal with radiation between the sample and its environment. Other facilities have implemented a guard surrounding the sample, as can be seen in Figure 3-2. This guard matches the temperature gradient of the sample and reduces the temperature difference between the two to almost zero. The current facility did not implement a guard as it was found to be unnecessary since the losses due to radiation were negligible compared to the other sources of uncertainty in the test set up. This was determined by performing a conservative calculation on maximum heat leak that could occur due to radiation. For this calculation, the assumed sample surface emissivity was unity and the sample radiates from 40 K to 4 K which results in a heat leak of $2.495E-4$ W. This was a conservative estimation as the temperature difference between the sample and the stage and shield was never this large; the stage and shield temperatures track with the sample temperature due to how heat was applied during testing.

3.2.2 Data Collection Procedure

There are two key measurement techniques that have been used for thermal bulk conductivity tests. The first, and most traditionally used, is a differential measurement technique. This technique requires the

measurement of four distinct data points taken at roughly the same temperature but with an increasing heat transfer rate. This allows for a modified version of Fourier's law to be used,

$$k(\bar{T}) = \frac{L}{A} \frac{dQ}{d\Delta T} \quad 3-3$$

where ΔT is the temperature differential measured by the temperature sensors (K), L is the distance between temperature sensors (m), A is the cross-sectional area perpendicular to heat flow (m^2), and Q is the heat flux (W).

The advantage of this technique is that it eliminates the effect of absolute temperature uncertainty due to the sensor's calibration curves [5]. Therefore, according to Tuttle et. al. [5], there is less relative uncertainty in this differential measurement than for a single point measurement.

The second measurement procedure is a single point measurement technique. This was the technique that was used for these measurements; however, the method was modified to reduce the effect of the absolute temperature uncertainty coming from the calibration curves. This measurement technique was used instead of the differential technique to simplify the automation of the test procedure.

The modification of the single point measurement technique resulted in a test procedure that occurs in two distinct steps. The first step is referred to as the parasitic test. The test was run by varying the chamber temperature using a heater mounted on the cold head, the trim heater, and recording the temperature difference between the two sensors mounted on the sample. The purpose of this step was to remove any parasitic temperature differences between the two sensors that were inherent to the test set up itself. At the same time, this process also removes the absolute temperature uncertainty of the measurement as it eliminates any temperature difference not due to the heat flux applied by the main heater. The second step is referred to as the main test. In this step, the full test was run. A non-zero heat flux was applied to the sample and the temperature difference that occurs from this heat flux was measured. The parasitic temperature difference measured in the initial step was then subtracted from this temperature difference resulting in a temperature difference caused solely by the applied heat. This temperature difference was

used in Fourier's Law, Equation 3-1, to determine the thermal bulk conductivity of the sample. For a more comprehensive outline of this data collection process, refer to Appendix A: Thermal Bulk Conductivity Procedure & Data Processing.

3.3 Calculations and Uncertainty Analysis

A single point absolute measurement technique was utilized, so Fourier's law, which can be seen in Equation 3-1, was used to determine the thermal bulk conductivity of the samples.

To determine the uncertainty in this measurement, the uncertainty from the measured variables in the system was propagated through the thermal bulk conductivity equation. Two different types of error were considered and will be classified as accuracy uncertainty and precision uncertainty. In this case, accuracy uncertainty was the uncertainty that occurs from the experimental set-up or from the equipment used in the system itself. Precision uncertainty, in this case, was the uncertainty associated with the variation observed between successive measurements under the same conditions. These two types of uncertainty were combined for each variable in Fourier's Law and these values were propagated through the equation to determine the uncertainty of the thermal bulk conductivity measurement itself.

3.3.1 Thermal Bulk Conductivity Total Uncertainty

The total thermal bulk conductivity uncertainty was calculated using Equation 3-4. The determination of the uncertainties in this equation can be found in the following sections. The partial derivatives of each of the variables found in Equation 3-4 are listed below in Equation 3-5 through Equation 3-9.

$$U_k = \sqrt{\left(\frac{\partial k}{\partial Q} U_Q\right)^2 + \left(\frac{\partial k}{\partial L} U_L\right)^2 + \left(\frac{\partial k}{\partial A} U_A\right)^2 + \left(\frac{\partial k}{\partial T_1} U_{T1}\right)^2 + \left(\frac{\partial k}{\partial T_2} U_{T2}\right)^2} \quad 3-4$$

$$\frac{\partial k}{\partial Q} = \frac{L}{A(T_1 - T_2)} \quad 3-5$$

$$\frac{\partial k}{\partial L} = \frac{Q}{A(T_1 - T_2)} \quad 3-6$$

$$\frac{\partial k}{\partial A} = -\frac{QL}{A^2(T_1 - T_2)} \quad 3-7$$

$$\frac{\partial k}{\partial T_1} = -\frac{QL}{A(T_1 - T_2)^2} \quad 3-8$$

$$\frac{\partial k}{\partial T_2} = \frac{QL}{A(T_1 - T_2)^2} \quad 3-9$$

3.3.2 Temperature Sensor Uncertainty

There were three different components of accuracy uncertainty that were present for the temperature sensors. These include measurement resolution, electronic uncertainty of the temperature monitor, and the calibration curve uncertainty. The Lake Shore 218 temperature monitor's electronic accuracy and measurement resolution for negative temperature coefficient RTDs are listed in resistance units in Equation 3-10 and 3-11 respectively [8].

$$U_{T,218m} = 0.050 [\Omega] \quad 3-10$$

$$U_{T,218e} = 0.8 [\Omega] + 0.04\% RDG \quad 3-11$$

In Equation 3-11, the symbol *RDG* represents the resistance reading of the sensor in ohms.

For the Cernox sensors utilized in this experiment, T1 and T2, the resistance equations can be expressed in temperature units utilizing the R-T relationships of each sensor. These equations can be found in Equations, 3-12 through 3-14. In the equations, *T* indicates the recorded temperature measurement in Kelvin.

$$U_{T,218m,cernox} = (7E - 6)T^2 - 0.0003T + 0.0022 \quad 3-12$$

$$U_{T,218e,cernox} = (5E - 5)T^2 + 0.001T - 0.0029 \quad 3-13$$

$$U_{T,calib,cernox} = (1E - 9)T^3 - (4E - 7)T^2 + 0.0002T + 0.0037 \quad 3-14$$

For Cernox temperature sensor T2, because it was calibrated against the reference temperature sensor T1, there was an additional uncertainty factor from this recalibration that was accounted for. This

can be seen in Equation 3-15. The value was a constant as the recalibration uncertainty was found to not change as a function of temperature.

$$U_{T,recalib,T2} = 0.0057 [K] \quad 3-15$$

In addition to accuracy uncertainty, each temperature sensor has its own precision uncertainty. Precision uncertainty was determined by measuring 200 data points, for each individual temperature measurement, and finding the average and standard deviation. Equation 3-16 was then used to calculate the precision uncertainty. In the equation the constant was included to represent a 95% confidence interval.

$$U_{T,prec} = 1.96STDEV_T \quad 3-16$$

The accuracy and precision uncertainty values above were combined into a single value by using the root sum of squares method as the uncertainties were independent of one another. This can be seen in Equation 3-17.

$$U_T = \sqrt{(U_{T,218m})^2 + (U_{T,218e})^2 + (U_{T,calib})^2 + (U_{T,recalib,T2})^2 + (U_{T,prec})^2} \quad 3-17$$

3.3.3 Applied Heat Uncertainty

Heat flux applied to the bulk sample was determined through a 4-wire measurement. Two multimeters measure voltage drop to determine the power output of the heater. One multimeter measures the voltage drop across the heater and the other measures the voltage drop across a high precision shunt resistor which was used to back out current. From these measurements, the applied heat can be calculated as seen in Equation 3-18.

$$Q = VI = V_K \left(\frac{V_{HP}}{R_{shunt}} \right) [W] \quad 3-18$$

There were four components of accuracy uncertainty for the heater. Two of the components were the measurement uncertainty of the two multimeters and the third component was the uncertainty of the

shunt resistor. The value of each of these uncertainties can be determined using Equations 3-19 through 3-21.

$$U_{R_{shunt}} = 0.0004 [\Omega] \quad 3-19$$

$$U_{V_K} = 0.003V_K + 0.005 [V] \quad 3-20$$

$$U_{V_{HP}} = (4E - 5)V_{HP} + (7E - 6) [V] \quad 3-21$$

These components of accuracy uncertainty were then propagated through the heating power calculation, as seen in Equation 3-18. The propagation equation and the partial derivatives found in that equation can be seen in Equation 3-22 and Equations 3-23 through 3-25 respectively. In these equations, Q is the applied heat (W), V_K is the voltage measured across the heater (V), V_{HP} is the voltage measured across the shunt resistor (V), and R_{shunt} is the shunt resistor's resistance of 2 ohms.

$$U_{Q,meas} = \sqrt{\left(\frac{\partial Q}{\partial V_K} U_{V_K}\right)^2 + \left(\frac{\partial Q}{\partial V_{HP}} U_{V_{HP}}\right)^2 + \left(\frac{\partial Q}{\partial R_{shunt}} U_{R_{shunt}}\right)^2} \quad 3-22$$

$$\frac{\partial Q}{\partial V_K} = \frac{V_{HP}}{R_{shunt}} = \frac{V_{HP}}{2\Omega} \quad 3-23$$

$$\frac{\partial Q}{\partial V_{HP}} = \frac{V_K}{R_{shunt}} = \frac{V_K}{2\Omega} \quad 3-24$$

$$\frac{\partial Q}{\partial R_{shunt}} = -V_K \frac{V_{HP}}{(R_{shunt})^2} = -\frac{V_K V_{HP}}{(2\Omega)^2} \quad 3-25$$

The final component of accuracy uncertainty was a conservative estimate of the amount of heat leak from the sample due to radiation. This value can be seen in Equation 3-26.

$$U_{Q,para} = 2.495E - 4 W \quad 3-26$$

The precision uncertainty was calculated using the same method as the temperature readings, utilizing the standard deviation of 200 data points. The precision uncertainty was then calculated using Equation 3-27. In the equation the constant was included to represent a 95% confidence interval.

$$U_{Q,prec} = 1.96STDEV_Q \quad 3-27$$

The accuracy and precision uncertainty values above were combined into a single value using the same method as the temperature readings, the root sum of squares method. That can be seen in Equation 3-28.

$$U_Q = \sqrt{(U_{Q,meas})^2 + (U_{Q,Para})^2 + (U_{Q,Prec})^2} \quad 3-28$$

3.3.4 Length and Cross-Sectional Area Measurement Uncertainty

The distance between temperature sensors and the sample diameter were each measured five times with calipers. The value for accuracy uncertainty, precision uncertainty, and total uncertainty for the length measurement can be seen in Equations 3-29 through 3-31 respectively. The precision uncertainty was calculated using the same method as the heater readings but utilizes 5 data points instead of 200. In the precision uncertainty equation, the constant that was included in this case represents a 99% confidence interval as the confidence level for this measurement was higher.

$$U_{L,meas} = 0.00001 [m] \quad 3-29$$

$$U_{L,prec} = 2.5706STDEV_L \quad 3-30$$

$$U_L = \sqrt{(U_{L,meas})^2 + (U_{L,prec})^2} \quad 3-31$$

The value of accuracy uncertainty for the diameter measurement can be seen in Equation 3-32. This value was propagated through the cross-sectional area measurement of a circle. The cross-sectional area of a circle formula, the propagation equation, and the partial derivative found in the propagation equation can be seen in Equations 3-33 through 3-35 respectively.

$$U_D = 0.00001 [m] \quad 3-32$$

$$A = \frac{\pi D^2}{4} \quad 3-33$$

$$U_{A,meas} = \sqrt{\left(\frac{\partial A}{\partial D} 0.00001 [m]\right)^2} \quad 3-34$$

$$\frac{\partial A}{\partial D} = \frac{\pi D}{2} \quad 3-35$$

Like the length measurement, the precision uncertainty was calculated utilizing 5 data points instead of 200. In the precision uncertainty equation, the constant that was included in this case represents a 99% confidence interval as the confidence level for this measurement was once again higher. Equation 3-36 shows this calculation.

$$U_{A,prec} = 2.5706STDEV_A \quad 3-36$$

The accuracy and precision uncertainty values above were combined into a single value using the same method as the temperature readings, using the root sum of squares method. That can be seen in Equation 3-37.

$$U_A = \sqrt{(U_{A,meas})^2 + (U_{A,prec})^2} \quad 3-37$$

3.4 Results and Discussion

Thermal bulk conductivity tests were conducted on 11 different oxygen free high conductivity (OFHC) copper 101 samples. These samples were purchased at their test dimensions of 6 inches in length and a half inch in diameter. Having the samples arrive at their test dimensions was important to avoid machining on site, which may change the conductivity.

Five of the samples, sourced from Sequoia Brass & Copper [9], were tested by graduate student researcher, Kacie Salmon. As can be seen in Figure 3-5, the results of different samples from this batch were very similar. Across the temperature range, the results stayed within a very narrow band indicating that the conductivities were similar. Therefore, it was concluded that the behavior of the conductivity could be determined by testing fewer samples. As the experiment proceeded and additional vendors were selected,

three samples instead of five were tested. The results from the additional two vendors tested, McMaster-Carr [10] and Thyssen-Krupp [11], can be seen in Figure 3-6 and Figure 3-7 respectively.

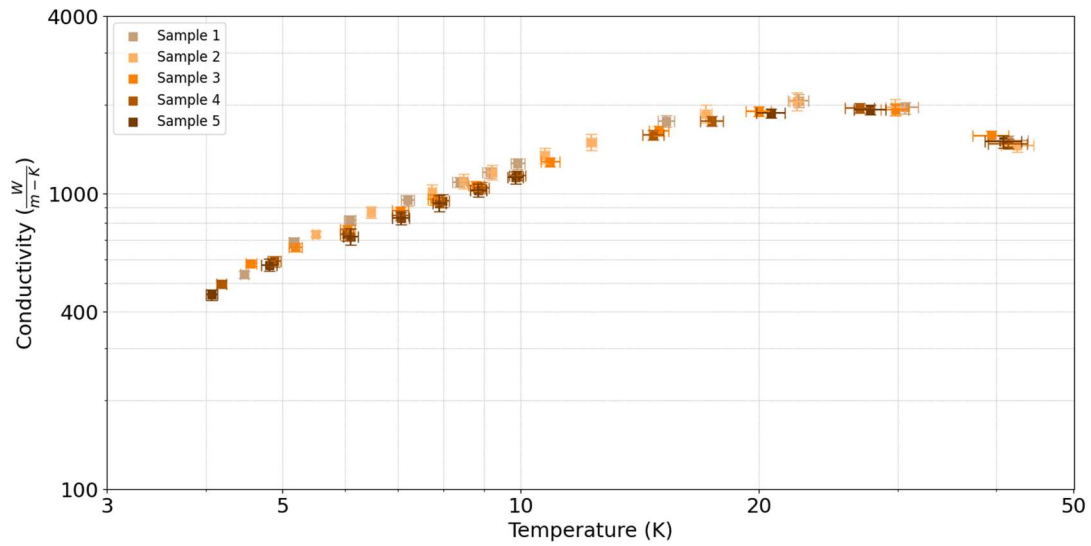


Figure 3-5. Thermal bulk conductivity results for samples sourced from Sequoia Brass & Copper.

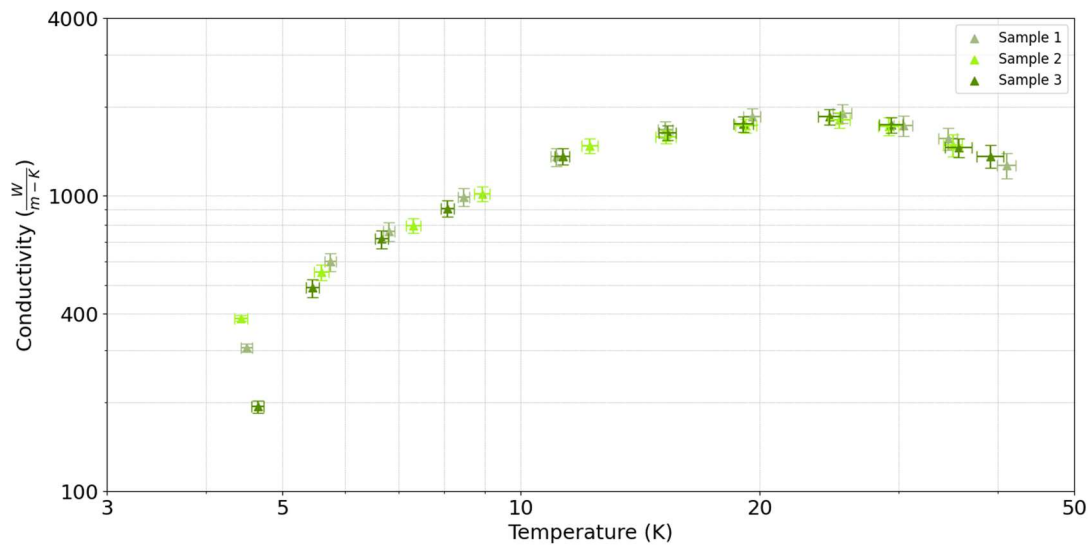


Figure 3-6. Thermal bulk conductivity results for samples sourced from McMaster-Carr.

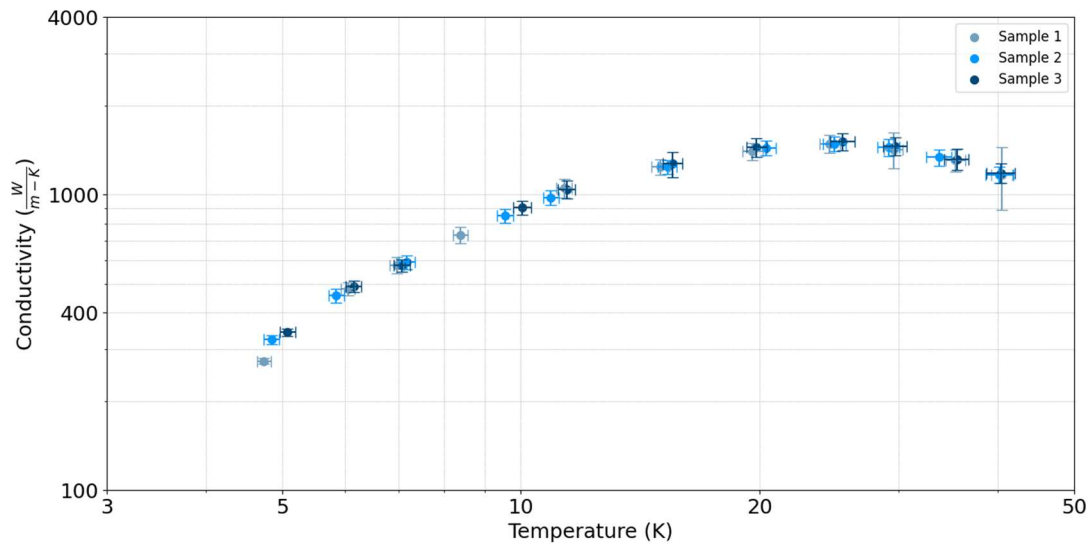


Figure 3-7. Thermal bulk conductivity results for samples sourced for Thyssen-Krupp.

3.4.1 Comparison with Literature

The purity of OFHC C101 copper rods is 99.99% [9]. For this level of purity, the expected RRR range is rather large. One source, Ekin et al. [7], states that the RRR for this copper is 50. Another source, Thermal Space, states the RRR value can be upwards of 500 [12]. This range is likely representative of the defect content of the material that can occur from differences in work hardening or annealing. At either end of this range, the thermal response of the copper differs vastly. This range was compared to the measured results in Figure 3-8.

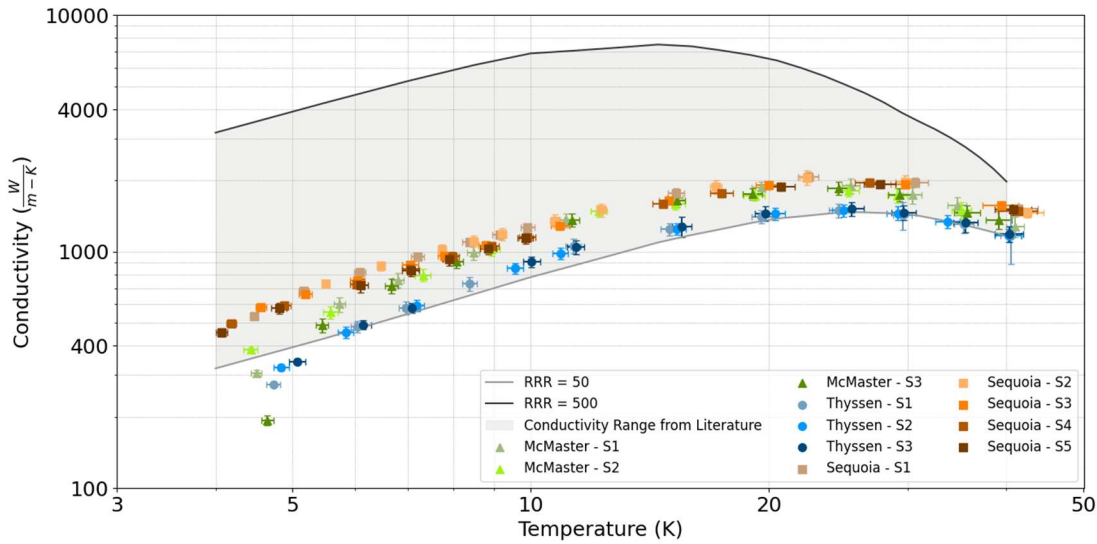


Figure 3-8. Comparison of measured data with known RRR curves from NIST [13].

3.4.2 RRR Determination

The National Bureau of Standards developed a function that relates RRR, thermal bulk conductivity, and temperature [14]. The equation was developed by fitting a function to 22 thermal bulk conductivity data sets from a variety of different sources. It is valid over a wide range of temperatures and RRR values, ranging from 0.2 K to 1250 K and 19 to 1800 respectively, and has an error of $\pm 10\%$. Equation 3-38 through 3-43 and a constant table, Table 3-1, compose this function.

$$\lambda = (W_o + W_i + W_{io})^{-1} \quad 3-38$$

$$W_o = \frac{\beta}{T} \quad 3-39$$

$$W_i = \frac{P_1 T^{P_2}}{1 + P_1 P_3 T^{(P_2 + P_4)} \exp\left(-\left(\frac{P_5}{T}\right)^{P_6}\right)} + W_c \quad 3-40$$

$$W_{io} = \frac{P_7 W_i W_o}{W_i W_o} \quad 3-41$$

$$\beta = \frac{\rho_o}{2.443E - 8} \quad 3-42$$

$$\beta_r = \frac{\beta}{0.0003} \quad 3-43$$

Table 3-1. Constants used in the function developed by The National Bureau of Standards.

Constant	Value
P ₁	1.754E-8
P ₂	2.763
P ₃	1102
P ₄	-0.165
P ₅	70
P ₆	1.756
P ₇	$\frac{0.838}{\beta_r^{0.1661}}$

In the equations and table above, λ is thermal bulk conductivity ($\frac{W}{m-K}$), ρ_o is residual electrical resistivity ($\frac{S}{m}$), T is temperature (K), ρ_{273} is the electrical resistivity of copper at 273 K ($\frac{S}{m}$), ρ_i are constants, and the remaining variables are intermediate calculations performed to obtain the thermal bulk conductivity.

Using this function, a more accurate determination of the RRR can be made in comparison to the graphical determination seen in Figure 3-8. The function was applied to each data point for all samples tested. The results were then averaged by sample and by vendor, which can be seen in Table 3-2.

Table 3-2. Sample average and vendor average RRR values.

Sample	Sample Average RRR Value	Vendor Average RRR
McMaster-Carr S1	72.1	

McMaster-Carr S2	68.4	
McMaster-Carr S3	70.1	70.2
Thyssen-Krupp S1	53.1	
Thyssen-Krupp S2	53.5	
Thyssen-Krupp S3	54.6	53.3
Sequoia Brass & Copper S1	83.6	
Sequoia Brass & Copper S2	83.6	
Sequoia Brass & Copper S3	79.4	
Sequoia Brass & Copper S4	76.4	
Sequoia Brass & Copper S5	75.2	79.6

In addition to using the function to determine the sample's average RRR value, it can also be used as a method to validate experimental results. The literature indicates that RRR value for a sample remains constant regardless of temperature, so comparing the RRR value of each individual data point to the sample average can be used to identify and remove outlier data points. This can be seen in Figure 3-9. In the figure, the lowest temperature data point is a clear outlier as it has a RRR value that is much lower than the sample average. A possible cause of the abnormally low conductivity value was an imperfect match of the temperature sensor's calibration curves resulting in a decrease in the ΔT measured; at these low temperatures, the measured ΔT was already small and any additional decrease could result the measured conductivity to deviate away from the sample average. A better estimate of the conductivity of the lowest

temperature data point at the temperature could be found by using the function and the sample's average RRR than from the test data.

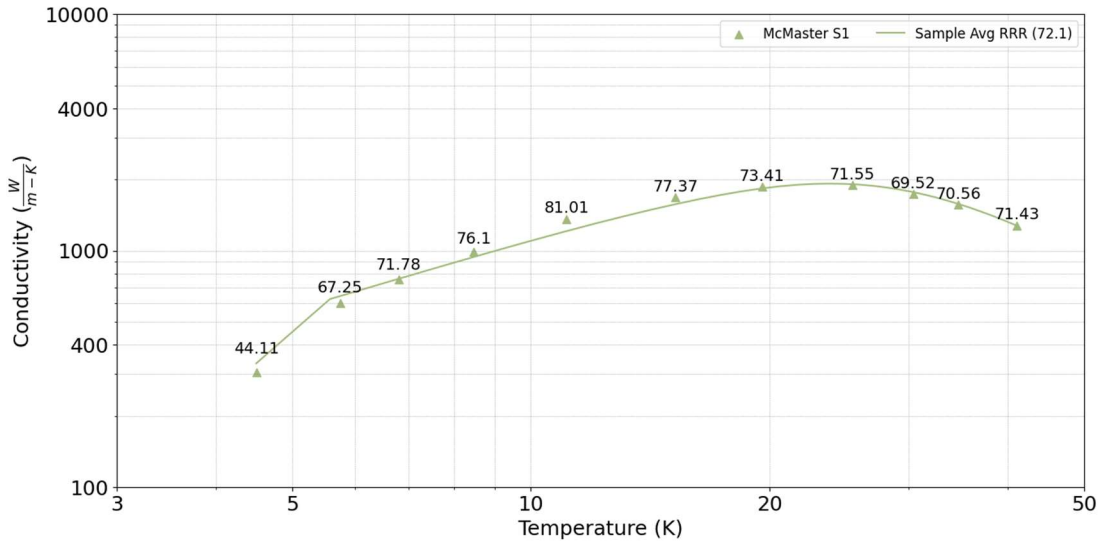


Figure 3-9. RRR value at each data point compared to the sample's average RRR value for McMaster-Carr sample 1.

3.5 Conclusions

Listed below are the main conclusions that have been drawn from the thermal bulk conductivity results:

1. Each vendor tested had its own unique average thermal bulk conductivity for its OFHC copper 101 samples. Samples from Sequoia Brass & Copper and McMaster-Carr were the most similar and had significantly higher conductivities than samples from Thyssen-Krupp. The difference between vendors was likely representative of the defect content of the material due to slight deviations in manufacturing methods.
2. Samples sourced from the same vendor and batch had thermal bulk conductivities that were more similar than samples sourced from different vendors. However, within the same vendor and batch there were still differences in thermal bulk conductivity of a few percent between samples. This is common and was also reported by Tuttle et. al. at NASA [5].

3. For OFHC copper 101 sourced directly from vendors, the RRR range can be narrowed down to a range between 50 and 80. If choosing a single value, the data suggests an RRR value of 75 would be reasonable.

4 Thermal Contact Resistance of Pressed Contacts

4.1 Literature Review

Thermal contact resistance is defined as the resistance to heat flow that occurs at the interface between two materials. The cause of this resistance is that the real area of contact between the two contacting surfaces is only a small fraction of the apparent contact area. The fraction of the apparent area that is in contact depends on several parameters including surface roughness, surface hardness, and contact pressure. A visual representation of this relationship can be seen in Figure 4-1.

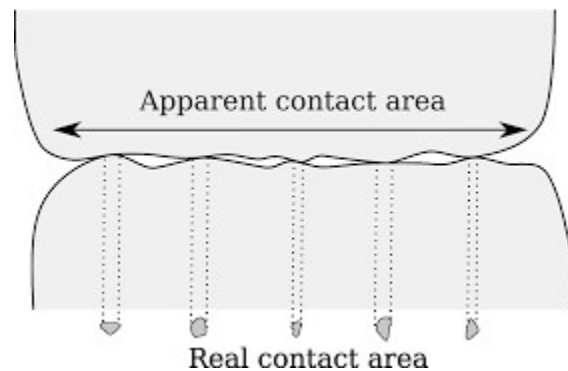


Figure 4-1. Relationship between apparent and real contact area [15].

Thermal contact resistance can be determined through the ratio between the temperature drop that occurs at the interface and the total heat flux applied. This calculation can be seen in Equation 4-1.

$$R = \frac{\Delta T}{Q} = \frac{\Delta T}{qA_c} \quad 4-1$$

where R is the total resistance at the interface ($\frac{K}{W}$), ΔT is the temperature drop across the interface (K), Q is the total heat flux (W), q is the area specific heat flux ($\frac{W}{m^2}$), and A_c is the cross-sectional area of the interface (m^2).

Conversely, thermal contact resistance can also be defined as its inverse, thermal contact conductance. Thermal contact conductance is defined as the measure of how well heat flows across an interface. This can be determined using Equation 4-2.

$$h = \frac{1}{RA_c} = \frac{q}{\Delta T} \quad 4-2$$

where h is area specific thermal contact conductance ($\frac{W}{K-m^2}$), R is thermal contact resistance, A_c is the cross-sectional area of the interface (m^2), q is the area specific heat flux ($\frac{W}{m^2}$), and ΔT is the temperature drop across the interface (K).

At an interface there are three components to the thermal contact conductance. The first, h_c , is the thermal conduction between contacting surfaces or interface materials. The second, h_g , is the conduction between gas-filled gaps between the contacting surfaces. The third, h_r , is thermal radiation between the two contacting surfaces. Because all of the contributions act independently from one another, they can be combined to determine the total contact conductance as seen in Equation 4-3 [16].

$$h = h_c + h_g + h_r \quad 4-3$$

For many cryogenic systems, including the system used in this work, only the conductance due to conduction, h_c , has an impact on the overall conductance. Conductance due to convection, h_g , can be dismissed as the system is held in a vacuum. Conductance due to radiation, h_r , can be dismissed due to the low temperatures of the system and the small temperature difference across the interface.

4.1.1 Factors that impact thermal contact resistance

There are many different factors that influence the thermal contact resistance of a joint. These factors consist of both material properties of the joined materials as well as external parameters. A comprehensive list of the important parameters is listed below [17].

Pressure

Pressure at the contact interface has been found to significantly affect thermal contact resistance. As pressure increases, not only do the existing contact points grow in area, but due to a reduction in gap area, additional asperities come into contact.

Interstitial Material

Interstitial materials are materials inserted between surfaces in contact to either increase or decrease the thermal contact resistance at the interface. The interstitial materials do this by having a different value of conductivity than that of the contact materials and by changing the overall area of contact. An additional effect of some interstitial materials is the prevention of oxidization at the interface.

Surface Topology

Surface topology controls how well the surfaces fit together; this affects the real area of contact and gap distance. Some of the important surface parameters include the surface roughness, R_a , flatness deviation, FD , and the slope of the asperities, m or m' .

Thermal Conductivity

The thermal conductivity of the contacting materials, and the thermal interface materials if present, impact the thermal contact resistance at the interface. If the interface consists of two different materials, the effective conductance is determined using Equation 4-4.

$$k_s = \frac{2k_1k_2}{k_1 + k_2} \quad 4-4$$

where k_s is the effective conductance ($\frac{W}{m-K}$), k_1 is the conductance of material 1 ($\frac{W}{m-K}$), and k_2 is the conductance of material 2 ($\frac{W}{m-K}$).

Modulus of Elasticity

The modulus of elasticity affects the elastic deformation of the contacting materials. This has an impact on the real area of contact of the interface.

Hardness and Yield Strength

The hardness and yield strength influence the plastic deformation of the asperities of the softer material in contact. This has an impact on the real area of contact of the interface.

Linear Coefficient of Thermal Expansion

The expansion or contraction of joined material can lead to a change in contact pressure or could result in the formation of a gap. Additionally, this expansion or contraction may lead to the formation of stresses within the material.

Average Interface Temperature

The temperature at the interface impacts the thermal and mechanical properties of the materials in contact. Many of these properties are strongly dependent on temperature, so the interface temperature has a significant effect on thermal contact resistance.

4.1.2 Models for thermal contact resistance

Numerous models have been created to determine thermal contact resistance from common and easily measurable interface and material properties. These models, which are continuously being created and updated in the literature, are constructed through analytical and empirical studies.

Generally, these models are categorized into two different cases. The first case assumes that the interface deforms elastically. The second case assumes that the interface deforms plastically. To determine which set of models is best suited for a specific contact scenario, a plasticity index is used. One such model was created by Greenwood and Williamson [18] and can be seen in Equation 4-5.

$$\psi = \frac{E'}{10H} \sqrt{\frac{\sigma}{\beta}} \quad 4-5$$

where ψ is the plasticity index (—), H is the hardness (Pa), σ is the surface roughness (μm), β is the radius of the asperities (μm), and E' can be determined using Equation 4-6.

$$\frac{1}{E'} = \frac{1 - \nu_1^2}{E_1} + \frac{1 - \nu_2^2}{E_2} \quad 4-6$$

where E' is the plane-stress modulus (Pa), ν_i is Poisson's ratio for the material on either side of the contact ($-$), and E_i is the modulus of elasticity for the material on either side of the contact (Pa).

The behavior of the contact, whether it behaves elastically or plastically, is determined based on the value obtained from the plasticity calculation. For values below 0.6 it can be assumed that the contact will behave elastically. For values greater than 1, it can be assumed that the contact will behave plastically. For values between 0.6 and 1 there is some uncertainty of the mode of deformation [19].

The following sections outline a single model for each of the two cases. There are many models that have been constructed for each case, but for the sake of conciseness in this report, only two will be described here. It is important to note that these models determine the contact conductance at the interface; to determine the thermal contact resistance from the contact conductance, Equation 4-2 should be used.

4.1.2.1 Elastic Models

Elastic models are generally dependent on the modulus of elasticity of the contacting materials. This is true for the model that will be described here, which was developed analytically by Mikic. This model can be seen in Equation 4-7.

$$h_c = 1.55 \frac{k_s m_s}{\sigma_s} \left(\frac{P\sqrt{2}}{E' m_s} \right)^{0.94} \quad 4-7$$

where h_c is thermal contact conductance ($\frac{W}{K-m^2}$), k_s is the effective thermal conductivity which can be determined using Equation 4-4 ($\frac{W}{K-m}$), m_s is the effective mean asperity slope which can be determined using Equation 4-8 (μm), σ_s is the effective RMS surface roughness which can be determined using Equation 4-9 (μm), P is pressure (Pa), and E' is the plane-stress modulus which can be determined using Equation 4-6 (Pa).

$$m_s = (m_1^2 + m_2^2)^{1/2} \quad 4-8$$

where m_s is the effective mean asperity slope and m is the asperity slope of the two materials.

$$\sigma_s = (\sigma_1^2 + \sigma_2^2)^{1/2} \quad 4-9$$

where σ_s is the effective RMS surface roughness (μm) and σ is the RMS surface roughness of the two materials (μm).

Mikic concluded that h_c is weakly dependent on m_s ($h_c \sim m_s^{0.06}$), so the equation could be simplified by using the average effective mean asperity slope for blasted surfaces, $m_s = 0.1$. This simplified version can be seen in Equation 4-10.

$$h_c = 1.9 \frac{k_s}{\sigma_s} \left(\frac{P}{E'} \right)^{0.94} \quad 4-10$$

One benefit to this formula is it is very practical to use. Only the RMS surface roughness and pressure need to be measured, assuming properties of the materials are known.

4.1.2.2 Plastic Models

Plastic models are generally dependent on the surface hardness, H_c , of the contacting materials. This is true for the theoretical framework model that was created by Cooper, Mikic, and Yovanovich, that was then correlated to experimental data by Yovanovich. The final form of this equation can be seen in Equation 4-11. This equation is valid for $10^{-6} \leq \frac{P}{H_c} \leq 2.3 * 10^{-2}$.

$$h_c = 1.25 \frac{k_s m_s}{\sigma_s} \left(\frac{P}{H_c} \right)^{0.95} \quad 4-11$$

4.1.3 Measurement techniques

There are two general measurement techniques used to determine thermal contact resistance, a transient method and a steady-state method. The steady-state method is much more commonly used, but both measurement techniques are described below.

4.1.3.1 Transient method

The transient method involves solving an inverse heat conduction problem (IHCP) to determine the thermal contact resistance at the interface. Essentially the surface heat flux and surface temperature

histories can be determined from the transient temperature measurements at one or more interior locations [20].

To obtain the transient temperature measurements a few methods have been proposed, two methods are described here. The first is to apply a transient pulse of heat to one side of the interface [21]. This pulse of heat flows across the contact interface and allows transient measurements of the temperature difference across the contact interface to be obtained. The second is to start with the two surfaces at different temperatures. These surfaces are then brought into contact allowing for heat transfer across the interface [22].

The transient technique is rarely used in practice for a few reasons. First, IHCP problems are more difficult to solve than traditional direct problems. Second, the test procedures described above are much more difficult to perform than the steady state technique that is described in the section below.

4.1.3.2 Steady-State method

The steady-state method involves solving a direct heat transfer problem in that the heat flux and the temperature difference across the interface are directly measured or calculated. The direct heat transfer problem that is solved in order to determine thermal contact resistance at the interface can be seen in Equation 4-1.

To obtain the measurements needed to solve Equations 4-1, a specific test fixture has been used by almost all of the studies found in literature. This fixture is designed to apply a uniform pressure to two cylindrical samples mounted end to end. A heater is attached to the top sample which sends heat through the contact interface and to the heat sink attached to the bottom sample. Temperature sensors are mounted at equally spaced axial locations on both sides of the interface and are used to linearly extrapolate the temperature at both sides of the interface. The heat flux into the sample is generally a known input but does not always directly match the heat flux through the contact interface. Factors such as alternate conduction paths and radiation need to be considered and accounted for. An example of one version of this test fixture can be seen in Figure 4-2.

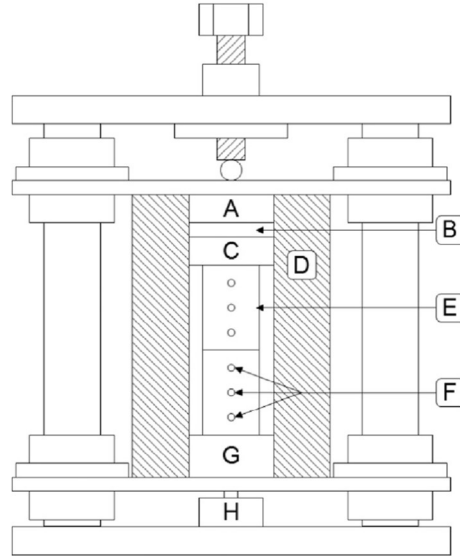


Figure 4-2. A pressed thermal contact resistance test fixture [21]. The letters in the figure correspond to key features; in this case, the three letters of importance are letters C, F, and G which correspond to the heater, linearly mounted temperature sensors, and heat sink respectively.

4.2 Test Methodology

4.2.1 Test Fixture

The thermal contact resistance measurements performed in this work were completed using the steady state measurement technique described above. The test fixture used was of a similar design to that used by Sponagle et. al. shown in Figure 4-2, but there were a few differences to some of the components of the design.

The test fixture used in this experiment can be seen in Figure 4-3. The test fixture was designed to be compatible with a similar sample geometry to that used in the thermal bulk conductivity tests. This allowed for both the reuse of the physical samples themselves and other fixture components, such as the heater and temperature sensor clamps.

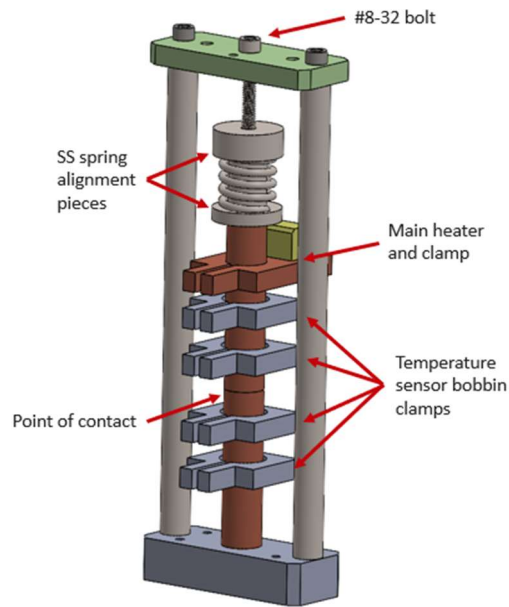


Figure 4-3. Thermal contact resistance test fixture design.

The fixture itself consists of a support structure that surrounds the two cylindrical samples that were pressed together end to end. The fixture was designed out of G10 (green) and stainless steel (grey) as these materials have low conductivity compared to the test specimens. This reduces the heat flow through this alternate heat path.

A uniform force was applied to the contact interface at ambient conditions prior to inserting the sample into the cryostat. The force was applied by turning an 8-32 bolt that compresses a linear spring that sits inside a stainless-steel housing designed to keep the spring centered and squared to the samples. A spring was used to apply the force due to the ease of application and measurement. The force was determined by measuring the linear distance traveled by the bolt after it makes contact with the spring. This linear distance can be determined by measuring the number of bolt rotations and using Equation 4-12.

$$L_{dist} = pN_{rot} \quad 4-12$$

where L_{dist} is the linear distance the bolt traveled (m), p is the pitch of the bolt (m), and N_{rot} is the number of rotations ($-$).

Knowing the change in spring length, Hooke's Law, Equation 4-13, was used to determine the applied force. This value of applied force was transformed into the pressure at the interface using Equation 4-14.

$$F_{spring} = k_{spring}L_{dist} \quad 4-13$$

where F_{spring} is the spring force (N), k_{spring} is the spring constant ($\frac{N}{m}$), and L_{dist} is the linear distance traveled by the bolt (m).

$$P = \frac{F_{spring}}{A_c} \quad 4-14$$

where P is the applied pressure (Pa), F_{spring} is the spring force (N), and A_c is the nominal cross-sectional area of the contact interface (m^2).

For the tests performed, two different springs were used to increase the range of pressures that could be achieved at the contact interface. Information about both springs can be seen in Table 4-1.

Table 4-1. Spring information.

	Spring Constant (N/m)	Free Length (m)	Fully Compressed Length (m)	Force Range (N)	Pressure Range (MPa)
Low Force Spring	28,896	0.0254	0.0169	0 – 261.1	0 – 13.30
High Force Spring	61,920	0.0275	0.0178	0 – 645.2	0 – 32.86

The force and pressure ranges that are found in Table 4-1 were not the direct values that would be obtained using Hooke's law. Adjustments to these ranges have been made to account for a few changes that occur during the cooldown process. The first change was a decrease in spring force due to thermal contraction differences between the sample path which includes the spring and the support structure. The sample path contracts 0.104 mm more than the support structure which results in a force reduction of 3.02 N when the low force spring was inserted and a force reduction of 6.44 N when the high force spring was

inserted. The second change was an increase in spring force due to an increase of the elastic modulus of the spring at low temperatures. A study in literature by Dillon et. al. applied this change of the elastic modulus directly to the change in force applied to the samples [23]. The same was done in this work, and it was found that the elastic modulus of the stainless-steel increased by roughly 8 percent resulting in an 8 percent increase in applied force [24].

4.2.2 Sample Preparation

Samples used in the thermal contact resistance tests were the same samples used in the thermal bulk conductivity tests. Upon completion of the thermal bulk conductivity tests, the 6-inch samples were shortened into two samples with a length of 2.25 inches.

The contact surfaces were prepared by first dry sanding the interfaces and then applying a layer of gold plating on top of this polished surface. The gold plating was outsourced to the company Incertec. There the gold plating with the following specifications was applied.

A soft gold plate with a maximum hardness of 90 HK₂₅ was applied to the surface with no underplating. The gold had a purity of 99.90% was applied with a minimum thickness of 1.25 μm and a maximum thickness of 1.5 μm.

After the gold plating had been applied, surface imaging using an Alicona InfiniteFocus G4 was performed. The average RMS surface roughness was measured and was found to be 1.7 microns. The surface flatness was measured and was found to vary significantly across the contact interface, which can be seen in the surface profile measurement in Figure 4-4. Because of this deviation from flatness, there was a significant reduction in the area of contact between the two mating samples. This reduction of contact area was determined using FujiFilm pressure paper, as can be seen in Figure 4-5. The uniformity of the intensity of the color of the pressure paper indicates that the pressure at the contact surface varied by 10% or less.

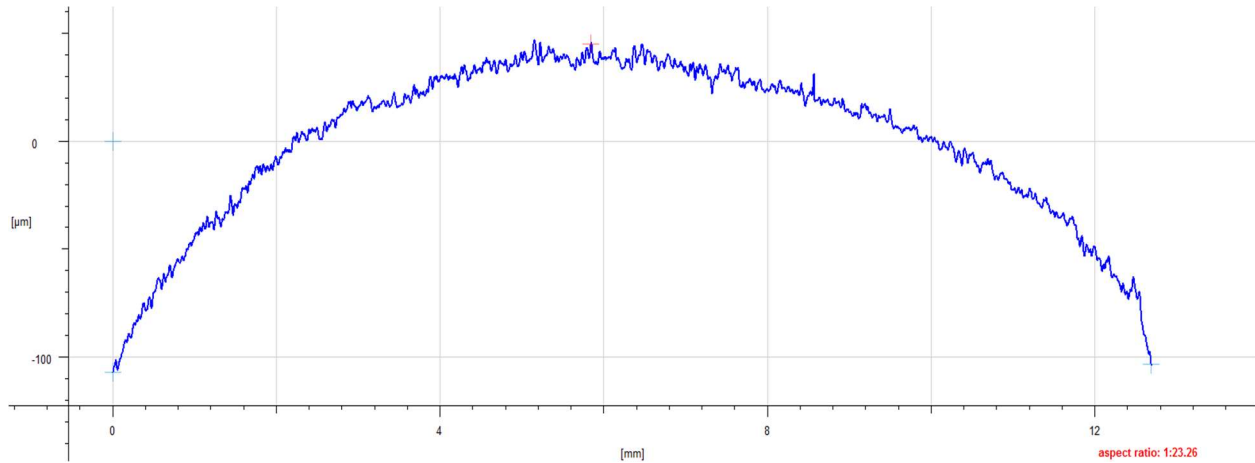


Figure 4-4. Surface profile along the diameter of the contact interface.

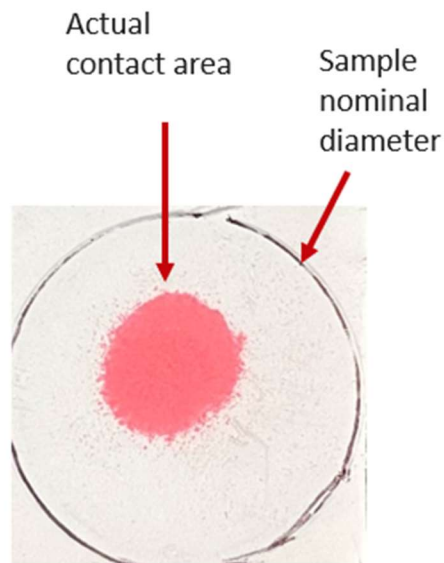


Figure 4-5. Contact interface pressure reading.

The impact of this area reduction was the introduction of an additional component of resistance due to the constriction of heat through a smaller area. This additional component of resistance was calculated using a correlation developed by Rohsenow et. al. [25] and in the end was found to be significant, impacting the thermal contact resistance by roughly 2 to 12 percent depending on the interface temperature and pressure. Because of this, the thermal contact resistance measurements in this work were adjusted, removing the effect of this constriction resistance.

4.2.3 Data Collection Procedure

4.2.3.1 Fixture Thermal Resistance Determination

Prior to performing any thermal contact resistance tests, the thermal resistance of the test fixture needed to be determined as an additional heat path was created due to the need to apply a clamping force to the samples. This determination of the thermal resistance of the test fixture allowed the determination of heat leak through the test fixture during the subsequent thermal contact resistance tests.

Determination of the thermal resistance of the test fixture required an additional test to be performed. Modifications to the test fixture were made for this test, which can be seen in Figure 4-6; the bottom sample was removed, and the top sample was supported with a G10 support and hollow G10 rods. This removes the heat path through the bottom sample and forces all of the heat to flow through the fixture.



Figure 4-6. Test fixture for fixture resistance determination.

Temperature was measured at the top and the bottom of the fixture heat path, as described by temperature sensors T3 and T4 in Figure 4-6. The thermal resistance of the fixture was then calculated using Equation 4-1.

The fixture resistance calculated using the method provided above was only valid at a specific average fixture temperature. This is due to the material properties of the G10 and Stainless-Steel changing as a function of temperature. To get the fixture resistance as a function of temperature, additional steps need to be taken. First, multiple fixture resistance measurements across the temperature range of interest need to be made. Then either a curve fit can be applied to these fixture resistance measurements or an effective $\frac{L}{A}$ technique can be used. In this work the effective $\frac{L}{A}$ technique was the method that was chosen and is described in more detail below.

To use the effective $\frac{L}{A}$ technique, it was assumed that the fixture resistance was dependent on the conductivity of the stainless-steel, as this was the material most of the fixture structure was composed of. The effective $\frac{L}{A}$ technique assumes a basic Fourier's law resistance through which the effective $\frac{L}{A}$ can be found by utilizing the integrated average conductivity of stainless steel over the ΔT measured by the two sensors located on the fixture. The effective $\frac{L}{A}$ value for each measurement can be determined using Equation 4-15.

$$R = \frac{L}{kA} = \frac{1}{k_{ss,intavg}} \left(\frac{L}{A}\right)_{effective} \quad 4-15$$

where R is the fixture resistance ($\frac{K}{W}$), L is the fixture length (m), k is thermal conductivity ($\frac{W}{m-K}$), A is the cross-sectional area of the fixture (m^2), and $k_{ss,intavg}$ is the integrated average conductivity of stainless steel ($\frac{W}{m-K}$).

The effective $\frac{L}{A}$ values determined from each measurement were then averaged and the resistance of the fixture was now solely a function of the temperature dependent conductivity of stainless-steel. For this work, two measurements were taken to determine the average effective $\frac{L}{A}$ value and the results of these

tests can be found in Table 4-2. It is important to note that this method only remains accurate if the effective $\frac{L}{A}$ values do not change drastically, as was true in this case.

Table 4-2. Data used to determine an average effective L/A value.

Thermal Bulk Conductivity Test Nominal Temperature Setting Matrix						
Data Point	Avg. T (K)	T3 (K)	T4 (K)	Int. Avg. k ($\frac{W}{m-K}$)	R ($\frac{K}{W}$)	L/A effective ($\frac{1}{m}$)
1	22.07	40.53	3.62	2.45	110.44	270.77
2	39.83	75.58	4.08	4.39	67.09	294.19
Average						282.48

Knowing the fixture resistance as a function of temperature, the amount of heat leak through the fixture can be determined when performing the thermal contact resistance tests. The ΔT across the fixture can be measured and the fixture resistance at the average fixture temperature can be calculated. Then, Equation 4-1 can be utilized to determine the heat leak.

4.2.3.2 Thermal Contact Resistance Procedure

Similar to the thermal bulk conductivity procedure, the thermal contact resistance tests were performed using a single point measurement technique. This test procedure also occurs in two distinct steps. The first step was the parasitic test. This test was run by varying the chamber temperature using a heater mounted on the cold head and recording the temperature differential between the temperature sensors mounted on the sample as well as on the fixture. The purpose of this step was to remove any parasitic temperature differences between the sensor locations that were inherent to the test set up itself. The second step was the main test. In this step the full test was run, a non-zero heat flux was applied to the heater mounted on the top sample and the temperature differences between the temperature sensors mounted on the sample as well as on the fixture were measured. The parasitic temperature difference measured in the initial step was then subtracted from this temperature difference resulting in a temperature difference caused solely by the applied heat. The data obtained from this step was used in a more complicated version of

Equation 4-1, that will be described in the subsequent calculation section, to calculate thermal contact resistance. For a more comprehensive outline of this data collection process, refer to Appendix B: Thermal Contact Resistance Procedure & Data Processing.

4.3 Calculations and Uncertainty Analysis

Generally, thermal contact resistance at an interface can be determined using the formula shown in Equation 4-1. However, In the case of this experiment, a few correction factors need to be added to the equation due to how the tests were performed. The resistance network shown in Figure 4-7 describes the sources of these additional terms added to the thermal contact resistance equation.

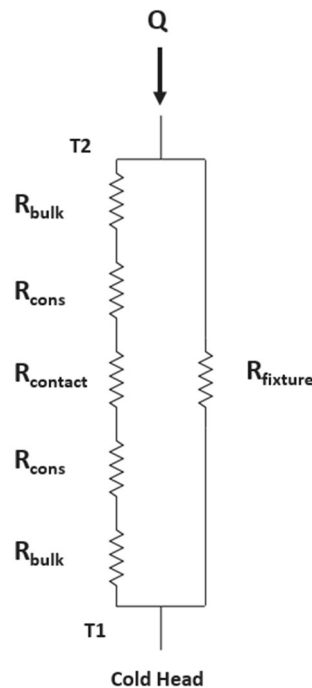


Figure 4-7. Resistance network of the thermal contact resistance test.

The first addition that needed to be made to the equation was a term to account for the heat flow through the fixture rather than the contact interface. The heat flow through the fixture was very minor due to its large resistance in comparison to the sample path, but there was still some heat flow through this path so it was accounted for. The second addition that needed to be made to the equation was to account for the temperature drop through the bulk material between the temperature sensor mounting locations and the

contact interface. This is shown in Figure 4-7 as the bulk resistances above and below the contact. To account for the temperature drop due to this bulk resistance, linearly mounted temperature sensors were utilized to extrapolate the temperatures at both sides of the contact interface. The temperature difference between the sensor measurement and the temperature at the contact interface was then removed. An example of this extrapolation can be seen in Figure 4-8. The third addition that needed to be made to the equation was to add an additional resistance term to account for the constriction of heat flow within the bulk material due to the reduced real area of contact at the interface. The constriction resistance was determined using a correlation developed by Rohsenow et. al. [25], outlined in Equation 4-16.

$$4kaR_{cons} = 1.08076 - 1.41042\varepsilon + 0.26604\varepsilon^3 - 0.0016\varepsilon^5 + 0.058266\varepsilon^7 \quad 4-16$$

where k is thermal bulk conductivity ($\frac{W}{m-K}$), a is the radius of the contact area (m), ε is the square root of the ratio between the contact area and sample area $\sqrt{\frac{A_c}{A}}$ (-), and R_{cons} is the constriction resistance ($\frac{K}{W}$).

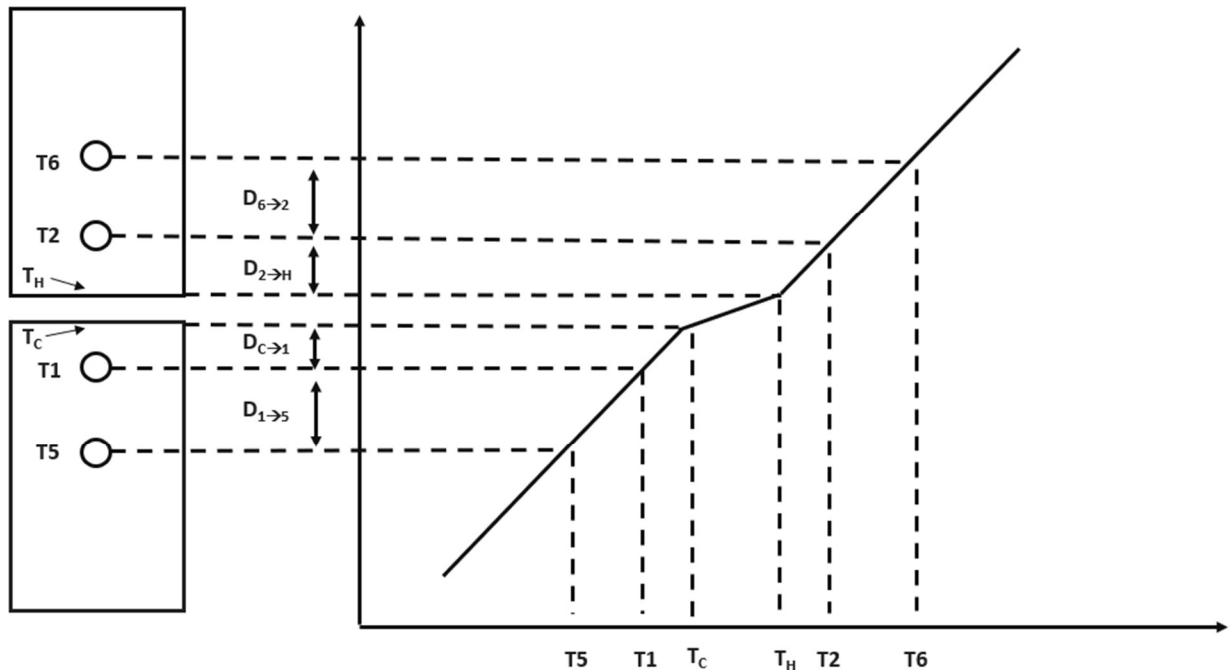


Figure 4-8. Contact interface temperature extrapolation.

The resulting changes to the generic thermal contact resistance equation due to the addition of these three correction factors can be seen in Equation 4-17.

$$R = \frac{T_2 - T_1 - \Delta T_{bulk}}{Q - Q_{fixture}} A_c - 2R_{cons} A_c \quad 4-17$$

where T_2 is the temperature measured by the sensor above the contact (K), T_1 is the temperature measured below the contact (K), ΔT_{bulk} is the temperature drop through bulk material (K), Q is the heat input from the heater (W), $Q_{fixture}$ is the heat that flows through the fixture (W), R_{cons} is the constriction resistance ($\frac{K}{W}$), and A_c is the cross-sectional area of the contact interface (m^2).

Like the thermal bulk conductivity uncertainty analysis, uncertainty from many different sources in the system was propagated through the thermal contact resistance equation. Two different types of error were considered and will be classified as accuracy uncertainty and precision uncertainty. These two types of uncertainty were combined for each variable in the thermal contact resistance equation and these values were propagated through the equation to determine the uncertainty of the thermal contact resistance measurement itself.

4.3.1 Thermal Contact Resistance Total Uncertainty

The total thermal contact resistance uncertainty was calculated using equation 4-18. The determination of the uncertainties located in this equation can be found in the following sections. The partial derivatives of each of the variables found in Equation 4-18 are listed below in Equation 4-19 through Equation 4-24.

$$U_R = \sqrt{\left(\frac{\partial R}{\partial Q} U_Q\right)^2 + \left(\frac{\partial R}{\partial Q_{fixture}} U_{Q_{fixture}}\right)^2 + \left(\frac{\partial R}{\partial \Delta T_{bulk}} U_{\Delta T_{bulk}}\right)^2 + \left(\frac{\partial R}{\partial T_1} U_{T_1}\right)^2 + \left(\frac{\partial R}{\partial T_2} U_{T_2}\right)^2 + \left(\frac{\partial R}{\partial A_c} U_{A_c}\right)^2 + \left(\frac{\partial R}{\partial R_{cons}} U_{R_{cons}}\right)^2} \quad 4-18$$

$$\frac{\partial R}{\partial Q} = -\frac{T_2 - T_1 - \Delta T_{bulk}}{(Q - Q_{fixture})^2} \quad 4-19$$

$$\frac{\partial R}{\partial Q_{fixture}} = \frac{T_2 - T_1 - \Delta T_{bulk}}{(Q - Q_{fixture})^2} \quad 4-20$$

$$\frac{\partial R}{\partial \Delta T_{bulk}} = -\frac{A_c}{(Q - Q_{fixture})} \quad 4-21$$

$$\frac{\partial R}{\partial T_1} = -\frac{A_c}{(Q - Q_{fixture})} \quad 4-22$$

$$\frac{\partial R}{\partial T_2} = \frac{A_c}{(Q - Q_{fixture})} \quad 4-23$$

$$\frac{\partial R}{\partial A_c} = \frac{T_2 - T_1 - \Delta T_{bulk}}{(Q - Q_{fixture})} - 2R_{cons} \quad 4-24$$

$$\frac{\partial R}{\partial R_{cons}} = 2A_c \quad 4-25$$

4.3.2 Temperature Sensor Uncertainty

There were three different components of accuracy uncertainty that were present for the temperature sensors. These components include measurement resolution, electronic uncertainty of the temperature monitor, and the calibration curve uncertainty. The Lake Shore 218 temperature monitor's electronic accuracy and measurement resolution for negative temperature coefficient RTDs are listed in resistance units in Equation 4-26 and Equation 4-27 respectively [8].

$$U_{T,218m} = 0.050 [\Omega] \quad 4-26$$

$$U_{T,218e} = 0.8 [\Omega] + 0.04\% RDG \quad 4-27$$

In Equation 4-27, the symbol *RDG* represents the resistance reading of the sensor in ohms. For the Cernox sensors utilized in this experiment - T1, T2, T3, and T6 - the resistance equations can be expressed in temperature units utilizing the R-T relationships of each sensor. The equations expressed in terms of temperature can be found in Equations, 4-28 through 4-30. For the Germanium sensors utilized in this experiment – T4 and T5 – the resistance equations can also be expressed in temperature units utilizing the R-T relationships of each sensor. The Germanium sensors each had unique R-T relations, so the values of the constants used for each sensor can be found in Table 4-3. The equations in terms of temperature for the

Germanium sensors can be seen in Equation 4-31 through Equation 4-33. In the equations, T indicates the recorded temperature measurement (K).

$$U_{T,218m,cernox} = (7E - 6)T^2 - 0.0003T + 0.0022 \quad 4-28$$

$$U_{T,218e,cernox} = (5E - 5)T^2 + 0.001T - 0.0029 \quad 4-29$$

$$U_{T,calib,cernox} = (1E - 9)T^3 - (4E - 7)T^2 + 0.0002T + 0.0037 \quad 4-30$$

$$B_{218m,germ} = AT^B \quad 4-31$$

$$B_{218e,germ} = CT^B + 0.0004T \quad 4-32$$

$$B_{calib,germ} = \sqrt{(B_{218m,cernox})^2 + (B_{218e,cernox})^2 + (B_{calib,cernox})^2} \quad 4-33$$

Table 4-3. Germanium sensor coefficients for uncertainty equations.

Germanium Sensor Uncertainty Equations Coefficients			
Sensor	A	B	C
T4	3E-6	2.9448	4E-5
T5	6E-6	2.9982	4E-5

For all temperature sensors except T1, there was an additional uncertainty factor due to the recalibration of the sensor against T1. These values can be seen in Table 4-4. The values were constant as the recalibration uncertainty was found not to change as a function of temperature.

Table 4-4. Recalibration uncertainty values.

Sensor	Recalibration Uncertainty (K)
T2	0.0057
T3	0.00565
T4	0.00485
T5	0.00565
T6	0.0048

In addition to accuracy uncertainty, each temperature sensor has its own precision uncertainty. This precision accuracy was determined by measuring 200 data points and finding the average and standard deviation. Equation 4-34 was then used to calculate the precision uncertainty. In the equation the constant was included to represent a 95% confidence interval.

$$U_{T,prec} = 1.96STDEV_T \quad 4-34$$

The accuracy and precision uncertainty values above were combined using the root sum of squares method as the uncertainties were independent. This can be seen in Equation 4-35.

$$U_T = \sqrt{(U_{T,218m})^2 + (U_{T,218e})^2 + (U_{T,calib})^2 + (U_{T,recalib,T2})^2 + (U_{T,prec})^2} \quad 4-35$$

4.3.3 Temperature Drop Through Bulk Material Uncertainty

The uncertainty of the temperature drop through the bulk material can be determined by propagating the uncertainty of the length and temperature measurements through the linear fit used to extrapolate the temperature at the contact interface. This relationship was assumed to be linear due to the close proximity of the sensors and the interface, which keeps temperature similar, within a few tenths of a Kelvin, resulting in nearly constant thermal bulk conductivity. The linear fits for the temperature drop through the bulk material both above and below the interface can be seen in Equation 4-36 and Equation 4-37 respectively.

$$\Delta T_{bulk,top} = T_2 - \frac{(T_6 - T_2)}{(L_{T_6 \rightarrow T_2})} L_{T_2 \rightarrow Contact} \quad 4-36$$

$$\Delta T_{bulk,bottom} = T_1 + \frac{(T_1 - T_5)}{(L_{T_1 \rightarrow T_5})} L_{T_1 \rightarrow Contact} \quad 4-37$$

The total uncertainty equation for both portions of the temperature drop through bulk material can be seen in Equation 4-38 and Equation 4-39 respectively. The uncertainty values for the length and temperature measurements used in these equations can be found in their respective sections and the partial

derivatives for Equation 4-38 and Equation 4-39 can be found in Equation 4-40 through Equation 4-47 below.

$$U_{\Delta T_{bulk,top}} = \sqrt{\left(\frac{\partial U_{\Delta T_{bulk,top}}}{\partial T_2} U_{T_2}\right)^2 + \left(\frac{\partial U_{\Delta T_{bulk,top}}}{\partial T_6} U_{T_6}\right)^2 + \left(\frac{\partial U_{\Delta T_{bulk,top}}}{\partial L_{T_6 \rightarrow T_2}} U_{L_{T_6 \rightarrow T_2}}\right)^2 + \left(\frac{\partial U_{\Delta T_{bulk,top}}}{\partial L_{T_2 \rightarrow T_{Contact}}} U_{L_{T_2 \rightarrow T_{Contact}}}\right)^2} \quad 4-38$$

$$U_{\Delta T_{bulk,bottom}} = \sqrt{\left(\frac{\partial U_{\Delta T_{bulk,bottom}}}{\partial T_1} U_{T_1}\right)^2 + \left(\frac{\partial U_{\Delta T_{bulk,bottom}}}{\partial T_5} U_{T_5}\right)^2 + \left(\frac{\partial U_{\Delta T_{bulk,bottom}}}{\partial L_{T_1 \rightarrow T_5}} U_{L_{T_1 \rightarrow T_5}}\right)^2 + \left(\frac{\partial U_{\Delta T_{bulk,bottom}}}{\partial L_{T_1 \rightarrow T_{Contact}}} U_{L_{T_1 \rightarrow T_{Contact}}}\right)^2} \quad 4-39$$

$$\frac{\partial U_{\Delta T_{bulk,top}}}{\partial T_2} = 1 - \frac{1}{(L_{T_6 \rightarrow T_2})} L_{T_2 \rightarrow Contact} \quad 4-40$$

$$\frac{\partial U_{\Delta T_{bulk,top}}}{\partial T_6} = -\frac{1}{(L_{T_6 \rightarrow T_2})} L_{T_2 \rightarrow Contact} \quad 4-41$$

$$\frac{\partial U_{\Delta T_{bulk,top}}}{\partial L_{T_6 \rightarrow T_2}} = \frac{(T_6 - T_2)}{(L_{T_6 \rightarrow T_2})^2} L_{T_2 \rightarrow Contact} \quad 4-42$$

$$\frac{\partial U_{\Delta T_{bulk,top}}}{\partial L_{T_2 \rightarrow T_{Contact}}} = -\frac{(T_6 - T_2)}{(L_{T_6 \rightarrow T_2})} \quad 4-43$$

$$\frac{\partial U_{\Delta T_{bulk,bottom}}}{\partial T_1} = 1 + \frac{1}{(L_{T_1 \rightarrow T_5})} L_{T_1 \rightarrow Contact} \quad 4-44$$

$$\frac{\partial U_{\Delta T_{bulk,bottom}}}{\partial T_5} = -\frac{1}{(L_{T_1 \rightarrow T_5})} L_{T_1 \rightarrow Contact} \quad 4-45$$

$$\frac{\partial U_{\Delta T_{bulk,bottom}}}{\partial L_{T_1 \rightarrow T_5}} = -\frac{(T_1 - T_5)}{(L_{T_1 \rightarrow T_5})^2} L_{T_1 \rightarrow Contact} \quad 4-46$$

$$\frac{\partial U_{\Delta T_{bulk,bottom}}}{\partial L_{T_1 \rightarrow T_{Contact}}} = \frac{(T_1 - T_5)}{(L_{T_1 \rightarrow T_5})} \quad 4-47$$

The total uncertainty of the temperature drop through the bulk material can be determined by combining the uncertainties of the temperature drop above and below the contact. This can be seen in Equation 4-48.

$$U_{\Delta T_{bulk}} = \sqrt{(U_{\Delta T_{bulk,top}})^2 + (U_{\Delta T_{bulk,bottom}})^2} \quad 4-48$$

4.3.4 Constriction Resistance

Constriction resistance was determined using a correlation developed by Rohsenow et. al. [25]. The uncertainty in the determination of constriction resistance using this correlation was reported to be a maximum of 2 percent.

$$U_{R_{cons}} = 0.02R_{cons} \quad 4-49$$

4.3.5 Applied Heat Uncertainty

The heat flux applied to the sample was determined through a 4-wire measurement. Two multimeters measure voltage drop to determine the power output of the heater. One multimeter measures the voltage drop across the heater and the other measures the voltage drop across a high precision shunt resistor which was used to back out current. From these measurements, the applied heat can be calculated as seen in Equation 4-50.

$$Q = V * I = V_K \left(\frac{V_{HP}}{R_{shunt}} \right) [W] \quad 4-50$$

There were four components of accuracy uncertainty for the heater. Two of the components were the measurement uncertainty of the two multimeters and the third component was the uncertainty of the precision of the shunt resistor. The value of each of these uncertainties can be determined using Equations 4-51 through 4-53.

$$U_{R_{shunt}} = 0.0004 [\Omega] \quad 4-51$$

$$U_{V_K} = 0.003V_K + 0.005 [V] \quad 4-52$$

$$U_{V_{HP}} = 4E - 5V_{HP} + 7E - 6 [V] \quad 4-53$$

These components of accuracy uncertainty were then propagated through the heating power calculation, as seen in Equation 4-50. The propagation equation and the partial derivatives found in that

equation can be seen in Equation 4-54 and Equations 4-55 through 4-57 respectively. In these equations, Q is the applied heat (W), V_K is the voltage measured across the heater (V), V_{HP} is the voltage measured across the shunt resistor (V), and R_{shunt} is the shunt resistor's resistance of 2 ohms.

$$U_{Q,meas} = \sqrt{\left(\frac{\partial Q}{\partial V_K} U_{V_K}\right)^2 + \left(\frac{\partial Q}{\partial V_{HP}} U_{V_{HP}}\right)^2 + \left(\frac{\partial Q}{\partial R_{shunt}} U_{R_{shunt}}\right)^2} \quad 4-54$$

$$\frac{\partial Q}{\partial V_K} = \frac{V_{HP}}{R_{shunt}} = \frac{V_{HP}}{2\Omega} \quad 4-55$$

$$\frac{\partial Q}{\partial V_{HP}} = \frac{V_K}{R_{shunt}} = \frac{V_K}{2\Omega} \quad 4-56$$

$$\frac{\partial Q}{\partial R_{shunt}} = -V_K \frac{V_{HP}}{(R_{shunt})^2} = -\frac{V_K V_{HP}}{(2\Omega)^2} \quad 4-57$$

The fourth component of accuracy uncertainty was a conservative estimate of the amount of heat leak from the sample due to radiation. This value can be seen in Equation 4-58.

$$U_{Q,para} = 2.495E - 4 \text{ [W]} \quad 4-58$$

The precision uncertainty was calculated utilizing the standard deviation of 200 data points. The precision uncertainty can then be calculated using Equation 4-59. In the equation the constant was included to represent a 95% confidence interval.

$$U_{Q,prec} = 1.96STDEV_Q \quad 4-59$$

The accuracy and precision uncertainty values were combined into a single value using the root sum of squares method. That can be seen in Equation 4-60.

$$U_Q = \sqrt{(U_{Q,meas})^2 + (U_{Q,para})^2 + (U_{Q,prec})^2} \quad 4-60$$

4.3.6 Heat Flow Through Fixture Uncertainty

The uncertainty of the fixture heat flow consists of the propagation of the uncertainty of the individual components through the fixture heat flow equation. The fixture heat flow calculation can be seen in Equation 4-61.

$$Q_{fixture} = \frac{T_3 - T_4}{R_{fixture}} \quad 4-61$$

The total uncertainty of the fixture heat flow was determined using Equation 4-62. The partial derivatives for Equation 4-62 can be found in Equation 4-63 through Equation 4-65. The uncertainty values of the components can be found in their respective sections or for the case of $R_{fixture}$ was determined within a function in Python code that post processes the collected data.

$$U_{Q_{fixture}} = \sqrt{\left(\frac{\partial T_3}{\partial Q_{fixture}} U_{T_3}\right)^2 + \left(\frac{\partial T_4}{\partial Q_{fixture}} U_{T_4}\right)^2 + \left(\frac{\partial R_{fixture}}{\partial Q_{fixture}} U_{R_{fixture}}\right)^2} \quad 4-62$$

$$\frac{\partial T_3}{\partial Q_{fixture}} = \frac{1}{R_{fixture}} \quad 4-63$$

$$\frac{\partial T_4}{\partial Q_{fixture}} = -\frac{1}{R_{fixture}} \quad 4-64$$

$$\frac{\partial R_{fixture}}{\partial Q_{fixture}} = -\frac{T_3 - T_4}{(R_{fixture})^2} \quad 4-65$$

4.3.7 Length and Cross-Sectional Area Measurement Uncertainty

The distance between temperature sensors, the distance between temperature sensors and the contact interface, and the sample diameter were each measured five times with calipers. The value for accuracy uncertainty, precision uncertainty, and total uncertainty for the length measurement can be seen in Equations 4-66 through 4-68 respectively. The precision uncertainty was calculated using the same method as the heater readings but utilizes 5 data points instead of 200. In the precision uncertainty equation,

the constant that was included in this case represents a 99% confidence interval as the confidence level for this measurement was higher.

$$U_{L,meas} = 0.00001 [m] \quad 4-66$$

$$U_{L,prec} = 2.5706STDEV_L \quad 4-67$$

$$U_L = \sqrt{(U_{L,meas})^2 + (U_{L,prec})^2} \quad 4-68$$

The value of accuracy uncertainty for the diameter measurement can be seen in Equation 4-69. This value was propagated through the cross-sectional area measurement of a circle. The cross-sectional area of a circle formula, the propagation equation, and the partial derivative found in the propagation equation can be seen in Equations 4-70 through 4-72 respectively.

$$U_D = 0.00001 [m] \quad 4-69$$

$$A = \frac{\pi D^2}{4} \quad 4-70$$

$$U_{A,meas} = \sqrt{\left(\frac{\partial A}{\partial D} * 0.00001 [m]\right)^2} \quad 4-71$$

$$\frac{\partial A}{\partial D} = \frac{\pi D}{2} \quad 4-72$$

The precision uncertainty was calculated utilizing 5 data points instead of 200. In the precision uncertainty equation, the constant that was included in this case represents a 99% confidence interval as the confidence level for this measurement was once again higher. Equation 4-73 shows this calculation.

$$U_{A,prec} = 2.5706STDEV_A \quad 4-73$$

The accuracy and precision uncertainty values were combined into a single value using the root sum of squares method. That can be seen in Equation 4-74.

$$U_A = \sqrt{(U_{A,meas})^2 + (U_{A,prec})^2} \quad 4-74$$

4.4 Results and Discussion

The present study collected two distinct thermal contact resistance data sets. The first data set explored the impact of de-mating and re-mating the contact interface, while the second data set examined the effect of interface pressure without ever de-mating the surfaces.

The results of the de-mate and re-mate tests are visible in Figure 4-9. In the figure, the solid line corresponds to the average thermal contact resistance of the five tests conducted at each pressure, and the shaded region represents the 95 percent confidence interval corresponding to the average.

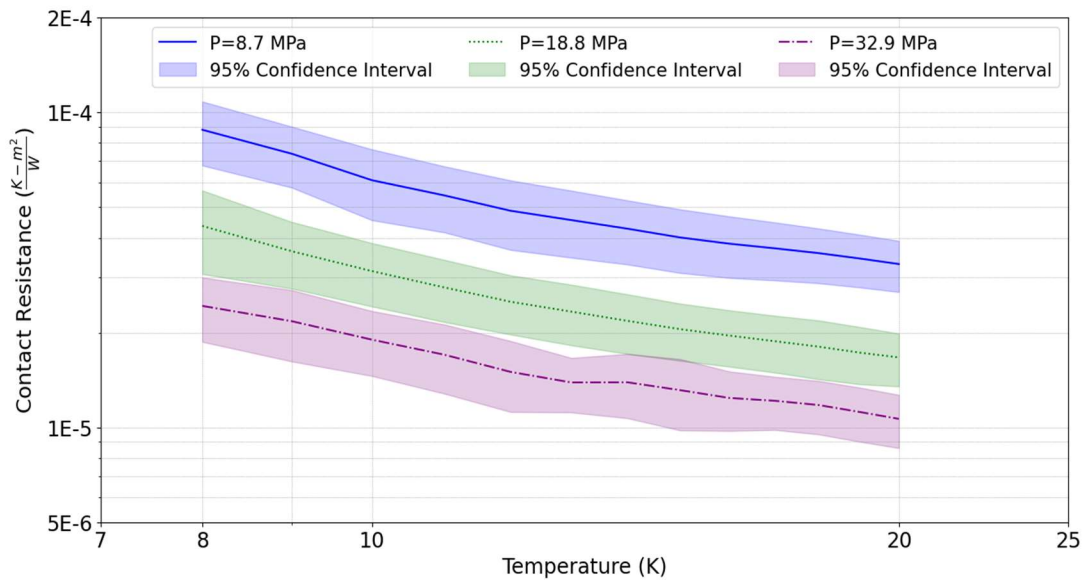


Figure 4-9. De-mate and re-mate thermal contact resistance results.

The results reveal significant variation in the measured thermal contact resistance resulting from de-mating and re-mating the contact interface. The width of the confidence intervals suggests that the relative variation remains consistent across the pressure range. This relative variation was approximately 22% for all pressure levels tested.

Figure 4-10 displays the results obtained without ever de-mating the surfaces. The tests covered a wide pressure range, from 1.26 MPa to 32.70 MPa. During the tests, a cylindrical clamp was employed to hold the contact interface in position between applications of force.

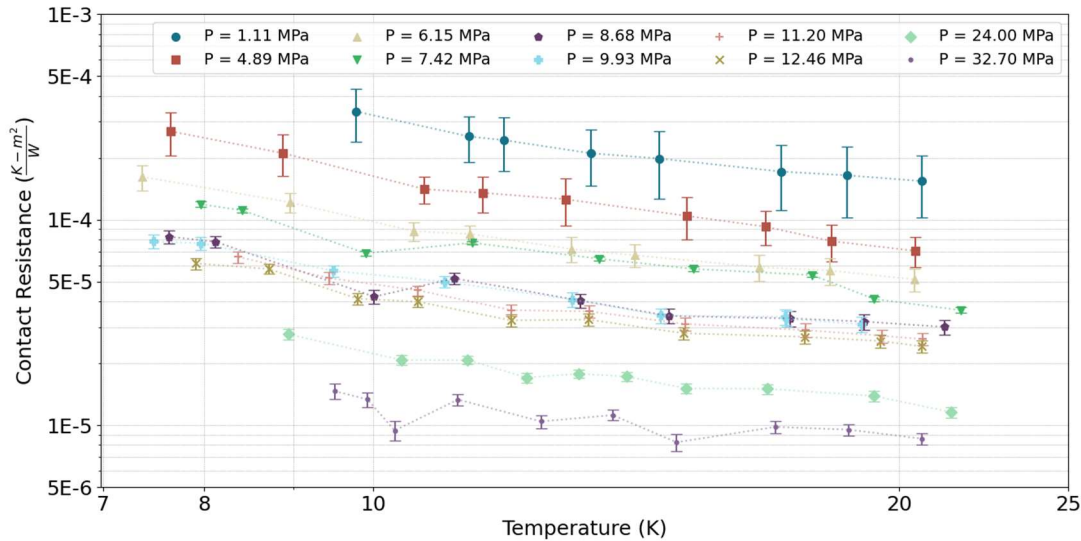


Figure 4-10. Thermal contact resistance results.

The measured data reveals that both temperature and pressure have an influence on the thermal contact resistance at the interface. Increasing the temperature at the interface leads to a decrease in thermal contact resistance. Similarly, increasing the pressure at the interface results in reduced thermal contact resistance.

A function was developed to fit this data. The function allows the determination of contact resistance associated with the tested surface conditions at a given temperature and pressure. The curve fit is given by Equation 4-75 through Equation 4-79. The curve fit was created from measured data ranging in temperature from 8 K to 20 K and pressure from 1.11 MPa to 32.70 MPa and is valid within those ranges. Additionally, the function extrapolates in a physically realistic way outside of this range for pressure specifically.

$$R_{contact} = Ae^{-P/B} + Ce^{-P/D} \quad 4-75$$

where $R_{contact}$ is area specific thermal contact resistance ($\frac{K-m^2}{W}$), P is pressure at the contact interface (Pa), and A through D are temperature-dependent coefficients.

$$A = a + \frac{b}{T} + \frac{c}{T^2} \quad 4-76$$

$$B = a + bT + cT^2 + \frac{d}{T} + \frac{e}{T^2} \quad 4-77$$

$$C = a + \frac{b}{T} + \frac{c}{T^2} \quad 4-78$$

$$D = a + bT + cT^2 \quad 4-79$$

where T is temperature (K), and letters a through e are constants that can be found in Table 4-5.

Table 4-5. Constants for the A-D constant curve fit equations.

Constant					
Undergoing	a	b	c	d	e
Curve Fit					
A	9.4313661E-05	-2.0996704E-03	1.5999077E-02		
B	7.8489461E+09	-3.7538249E+08	6.4679588E+06	-6.8871451E+10	2.1721198E+11
C	4.6951196E-04	-1.0337311E-02	9.6521076E-02		
D	-1.655485E+06	7.7061103E+05	-2.6556552E+04		

The developed function allowed for the investigation of characteristics that were difficult to see in the measured data, for example the rate of change of the contact resistance as a function of pressure. The rate of change can be better seen when contact resistance is plotted against pressure, determined by the function, which can be seen in Figure 4-11. For gold plated copper contacts there were diminishing returns in terms of the reduction in contact resistance past a certain interface pressure.

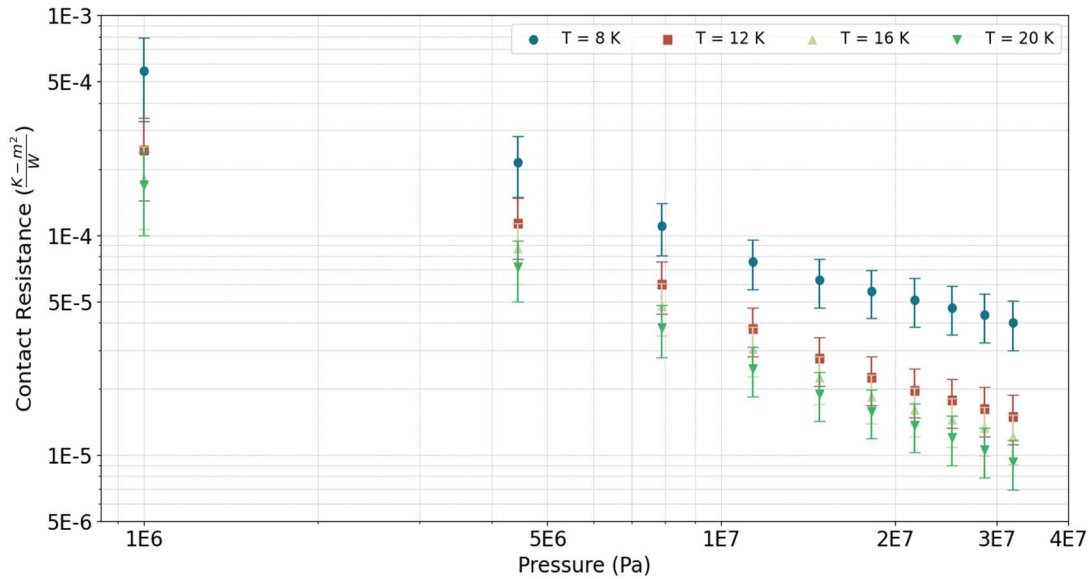


Figure 4-11. Thermal contact resistance data as a function of pressure. Determined from the function fit to the collected data.

The uncertainty of the function's calculated values is a combination of the uncertainty of the fit of the function itself and the uncertainty of the data the function was fit to. The sources of these components of uncertainty can be seen in Table 4-6. The combination of these sources results in an overall uncertainty of a contact resistance value calculated from the function that ranges from 25% to 45%.

Table 4-6. Contributing sources of uncertainty.

Source	Value
Measurement Uncertainty	6.6% at 32.70 MPa
	31.8% at 1.11 MPa
De-mate/Re-mate Uncertainty	22%
Function Fit Uncertainty	10.9%

Utilizing this function facilitated the comparison of the measured data with a similar dataset in the literature collected by Dillon et. al. [23] at identical pressures and temperatures. The results of this comparison are depicted in Figure 4-12, while a comparison of the material and surface conditions is provided in Table 4-7.

Table 4-7. Comparison of material and surface conditions.

	Measured Data	Literature Data
RRR of Bulk	75	125
Material		
Surface	1.7 μm	1.6 μm
Roughness		
Gold Plating Specifications	A soft gold plate, with a maximum hardness of 90 HK ₂₅ , was applied to the surface without any underplating. The gold, with a purity of 99.90%, was applied with a minimum thickness of 1.25 μm and a maximum thickness of 1.5 μm .	A gold plate, with a hardness range of 130-200 HK ₂₅ , was applied without any underplating. The gold, with a purity of 99.00%, was applied with a minimum thickness of 1.27 μm and a maximum thickness of 2.54 μm .
Contact Area	19.63 mm ²	232 mm ²

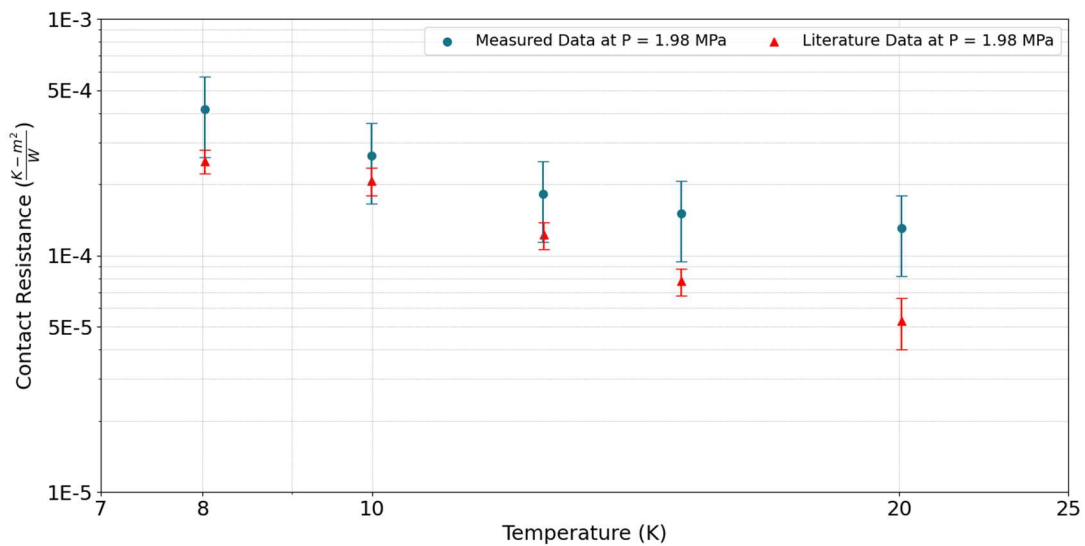


Figure 4-12. Comparison of measured data and literature data.

The data sets agree in both the overall trend of the data and in the magnitude of the reported values. The measured data reports contact resistance values that were on average 40% larger than those obtained from Dillon et al. [23]. The differences in the interface conditions between these tests were likely one cause of this discrepancy, specifically the increased conductivity of the bulk copper used by Dillon et al. [23] relative to the copper used here.

4.5 Conclusions

Listed below are the main conclusions that have been drawn from the thermal contact resistance results:

1. For the given interface conditions, as pressure and temperature increase the thermal contact resistance observed at the interface decreases. However, as pressure was increased passed a certain value, there were diminishing returns in the reduction of thermal contact resistance at the interface.
2. Variation of thermal contact resistance measurements due to the specific mate of the contact interface was investigated and the relative magnitude was found to be about 22 percent of the thermal contact resistance measured regardless of the temperature and pressure at the interface.
3. The function fit to the experimental data allows for the determination of the thermal contact resistance of a contact with specific surface conditions over a wide range of temperatures and pressures. The average uncertainty of the function itself was found to be 10.9 percent. If the function was used to determine thermal contact resistance values, the uncertainty of the function fit would be combined with the measurement and remate uncertainties resulting in a total uncertainty ranging from 25 percent to 45 percent.

5 The Thermal Optimization of a Bolted Joint

5.1 Literature Review

In practice, bolted joints are the most common types of mechanical connections used. The thermal resistance associated with these joints is an important consideration in the thermal analysis of an overall system. Knowing this, one may predict that there would be many studies that focus on the thermal behavior of these joints, however this is not the case. The lack of studies performed on bolted joints stems from the complexity that occurs due to the nonuniform pressure distribution the bolt imposes to the contact interface. This nonuniform pressure makes it difficult to determine the thermal contact resistance at the interface which subsequently makes it difficult to predict the total resistance of the joint.

From the small number of studies that have investigated the thermal resistance of bolted joints, two different methodologies have been used. The thermal contact resistance is specifically of interest as it is the thermal parameter of the joint that is unknown; the rest of the joint, mainly heat transfer through bulk material, can generally be predicted. The first method consists of manufacturing the bolted joint and performing physical tests in a cryostat. The second method consists of combining thermal contact resistance models created for uniform pressure conditions with mechanical models that predict pressure at the interface.

5.1.1 Physically Measuring Thermal Contact Resistance

There have been several experimental designs that focus on determining the thermal contact resistance distribution at the interface. Many of these designs measure the thermal contact resistance at a single point on the contact which is generally unhelpful. The experimental technique that will be discussed was performed by Hasselström et. al [16]; this technique proposes a methodology for determining the thermal contact resistance across the whole interface.

The test fixture used by Hasselström et. al. can be seen in Figure 5-1. Heat is inserted into the system via a polyimide heater mounted to the top surface of the upper plate using an adhesive layer. The applied heat flows through the contact interface held together by the bolt pattern being investigated and out

to the cold base plate. Located directly above and below the interface are thermocouples that are used to measure temperature at several radial distances from the bolt head.

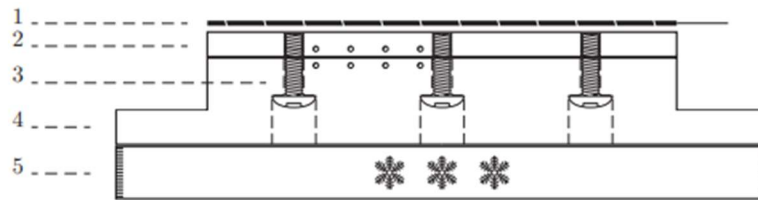


Figure 5-1. Illustration of the experimental setup for the bolted joint. 1-Heater, 2-Top Plate, 3-bolts, 4-Bottom plate, 5-Cold base plate.

The thermal contact resistance at the interface was determined by first estimating the thermal contact resistance distribution at the interface followed by using a numerical processor that solves a 3-dimensional temperature field for the given thermal contact resistance distribution. This temperature distribution was then compared to the temperature distribution that was found in the physical tests. If the solution did not converge, the process was repeated by updating the thermal contact resistance at the interface and again resolving the 3-dimensional temperature field.

Several different bolted connections were tested in order to investigate different contact parameters such as contact material, plate thickness, thermal interface material, number of bolts, etc. For each configuration, the entire geometry needed to be remade, which is the main drawback to this methodology. To perform any amount of joint optimization, a large number of tests would need to be run, and manufacturing all of those joints is very expensive and time consuming.

5.1.2 Using Models to Determine Thermal Contact Resistance

Many of the thermal contact resistance correlations found in the literature are a function of pressure at the interface. For ‘pressed’ or uniform interface pressure contacts these correlations can be directly applied, but due to the pressure variation at the interface of bolted contacts a second model is needed that describes the pressure field.

One such pressure model was developed by Fernlund [26] which reports the pressure as a conical distribution that is a function of radial distance from the bolt center and the depth beneath the bolt head. This model can be seen in Equation 5-1 through Equation 5-6 .

$$P(r, z) = Ar^4 + Br^3 + Cr^3 + D + E \quad 5-1$$

$$A(z) = \frac{\frac{15}{\pi} \left(\frac{2}{d}\right)^6 F}{-\left(\frac{2x}{d}\right)^6 + 2\left(\frac{2x}{d}\right)^5 + 5\left(\frac{2x}{d}\right)^4 - 20\left(\frac{2x}{d}\right)^3 + 25\left(\frac{2x}{d}\right)^2 - 14\left(\frac{2x}{d}\right) + 3} \quad 5-2$$

$$B(z) = -\frac{4}{3} \left(\frac{4x}{d} + 1\right) \frac{d}{2} A(z) \quad 5-3$$

$$C(z) = \frac{4x}{d} \left(\frac{2x}{d} + 2\right) \left(\frac{d}{2}\right)^2 A(z) \quad 5-4$$

$$D(z) = -2x^2 d A(z) \quad 5-5$$

$$E(z) = -\frac{1}{3} \left(\frac{2x}{d}\right)^3 \left(\frac{2x}{d} - 4\right) \left(\frac{d}{2}\right)^4 A(z) \quad 5-6$$

where F is force (N), d is the bolt shank diameter (m), r is the radial distance from the center of the bolt (m), z is the depth beneath the bolt head (m), P is the pressure at the specific radius and depth (Pa), and x is the radius of the stress zone that can be determined using Equation 5-7 (m).

$$x = \frac{d_s}{2} + z \tan(\alpha) \quad 5-7$$

where d_s is the bolt head diameter (m) and α is the cone angle.

Using Fernlund's model and coupling it with a thermal contact resistance model, for example those described in section 4.1.2, the thermal contact resistance at all interface locations can be determined. Generally, this process is not performed individually location by location, rather a program is used to determine the pressure distribution of the interface and then the thermal contact resistance correlation is applied.

5.2 Model Construction

The finite element simulation software ANSYS was utilized to optimize flat plate bolted contacts using data obtained in previous sections. The general configuration of the geometry that was simulated can be seen in Figure 5-2.

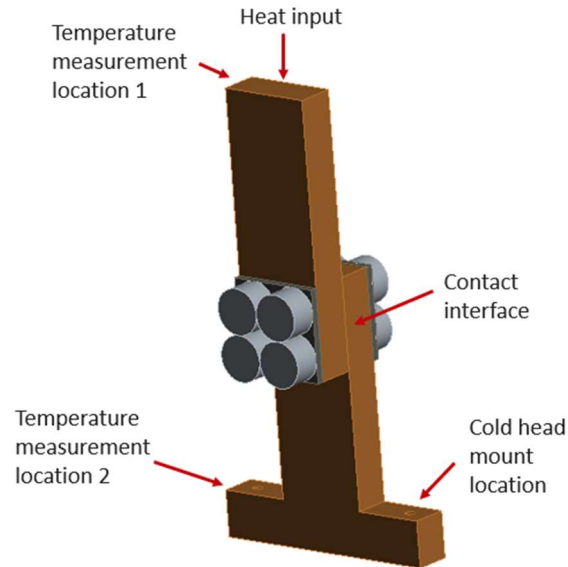


Figure 5-2. General geometry used in the simulations.

The geometry consisted of two gold-plated OFHC copper plates clamped together by a number of stainless-steel bolts. Thin plates manufactured from Invar were located within the clamped material. Invar, which experiences minimal contraction when cooled, balanced thermal contraction differences between the copper plates and stainless-steel bolts. This ensured the pretension applied to the bolts remained unchanged during the cooldown process. Identical thicknesses of the clamped material on both sides of the interface were chosen to position the contact interface at the midpoint of the bolt grip length. The midpoint was selected as it was the most favorable position regarding the distribution of pressure according to Fernlund's pressure cone model [26]. Dimensions of the contact interface and the entire geometry are outlined in Table 5-1 and Table 5-2.

Table 5-1. Contact interface dimensions.

Component	Dimension	Value
Contact Interface	Length	20 mm

	Width	20 mm
Number of Bolts		1+

Table 5-2. Geometry component dimensions.

Component	Dimension	Value
Copper Plates	Length	60 mm
	Width	20 mm
	Thickness	8.5 mm
Invar Plates	Length	20 mm
	Width	20 mm
	Thickness	1.5 mm
Metric Bolts		M2 – M16

To have the simulation match real-world behavior, bolt pretension was applied at room temperature, 293 K, prior to cooldown. This approach ensured the thermal contraction and subsequent thermal stresses in the model would match the conditions that would occur in practice. Upon reaching the 8 K setpoint condition, additional thermal boundary conditions were introduced. The cold head mounting location was set to 8 K, and a total heat input of 0.2 W was applied to the opposite end of the contact.

The thermal simulation associated with the heat load was decoupled from the mechanical simulation. The thermal contraction resulting from the heat load was insignificant relative to the thermal contraction accompanying the cool down and did not affect the contact interface pressure. Therefore, the pressure dependent thermal contact resistance correlation corresponding to the setpoint temperature was applied.

5.3 Simulation Design

Thermal optimization consisted of determining the bolt configuration that minimized the joint's overall resistance. This involved decomposing the joint's resistance into several components and performing simulations to identify each component individually. The three components that were investigated include

the resistance of the bulk material alone (excluding the contact interface or bolts), the resistance increase due to the bolts (excluding the contact interface), and the resistance increase due to thermal contact resistance. The resistance for each simulation component was determined using Equation 5-8.

$$R_{calculated} = \frac{\Delta T}{Q} \quad 5-8$$

where $R_{calculated}$ is the calculated resistance of the individual component of resistance ($\frac{K}{W}$), ΔT is the temperature difference across the entire joint (K), and Q is the heat input into the system (W).

The first source of resistance investigated was the resistance that is associated with the bulk material. To isolate this portion of resistance, a simulation was developed with a geometry that did not have bolts or a contact interface, which can be seen in Figure 5-3.

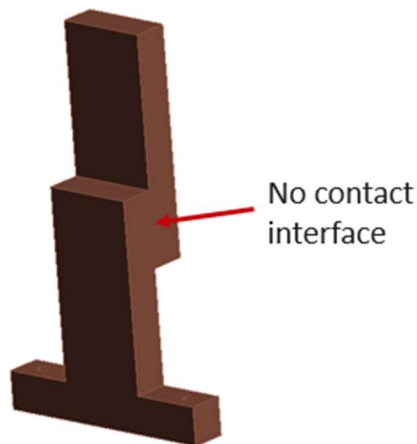


Figure 5-3. Simulation used to determine the portion of resistance caused by the bulk material.

$$R_{bulk} = R_{calculated} \quad 5-9$$

where R_{bulk} is the resistance that occurs within the bulk material ($\frac{K}{W}$).

The second source of resistance was related to the constriction of heat flow due to the reduction in area that occurs from the addition of bolts. The simulation used to examine this source of resistance included the bolt configuration but did not include any contact resistance at the interface, as shown in Figure 5-4.

The calculation used to determine the resistance caused by the reduction of area can be seen in Equation 5-10.

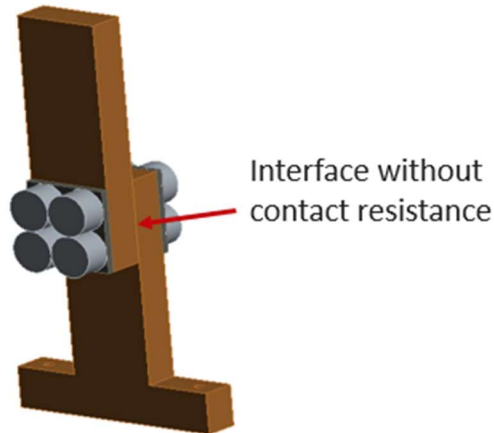


Figure 5-4. Simulation used to determine the portion of resistance due to contact area reduction.

$$R_{area\ reduction} = R_{calculated} - R_{bulk} \quad 5-10$$

where $R_{area\ reduction}$ is the resistance caused by the reduction in contact interface area $\left(\frac{K}{W}\right)$.

The third source of resistance investigated was related to contact resistance at the interface. This simulation included both the bolt configuration and the pressure dependent contact resistance at the interface, as shown in Figure 5-5. The calculation used to determine the resistance caused by contact resistance at the interface can be seen in Equation 5-11.

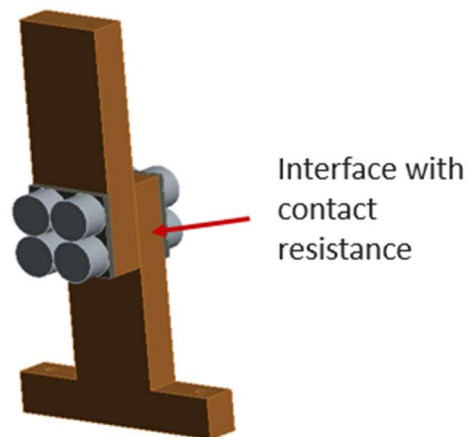


Figure 5-5. Simulation used to determine the portion of resistance due to thermal contact resistance.

$$R_{contact\ resistance} = R_{calculated} - R_{area\ reduction} - R_{bulk} \quad 5-11$$

where $R_{contact\ resistance}$ is the resistance caused by the thermal contact resistance at the interface ($\frac{K}{W}$).

The total resistance of the bolted connection was determined by combining the three components of resistance determined by the three simulations. This calculation can be seen in Equation 5-12.

$$R_{total} = R_{bulk} + R_{area\ reduction} + R_{contact\ resistance} \quad 5-12$$

where R_{total} is the total resistance of the bolted joint ($\frac{K}{W}$).

5.4 Results and Discussion

Prior to performing any simulations, a mesh dependency study was conducted. From the results of the study, the total resistance of the contact remains constant when the size of the mesh elements was smaller than 1E-3 meters for all contacts simulated. Four different bolt configurations were investigated, depicted in Figure 5-6. For each of these bolt configurations, simulations were performed with bolts of varying sizes. In all of the simulations preloaded the bolts to their maximum recommended value, as per Shigley's recommendations [27], to achieve an optimal thermal contact resistance distribution at the interface. The preload for each bolt size was determined using Equation 5-13. The results of all bolt configurations are depicted in Figure 5-7 through Figure 5-10.

$$F_{PL} = 0.64S_{ty}A_t \quad 5-13$$

where F_{PL} is the preload force (N), S_{ty} is tensile yield strength (Pa), and A_t is the tensile stress area which is calculated using Equation 5-14 (m^2).

$$A_t = \frac{\pi}{4}(d_{nom} - 0.9382P)^2 \quad 5-14$$

where d_{nom} is the nominal (major) bolt diameter (mm) and p is the thread pitch (mm).

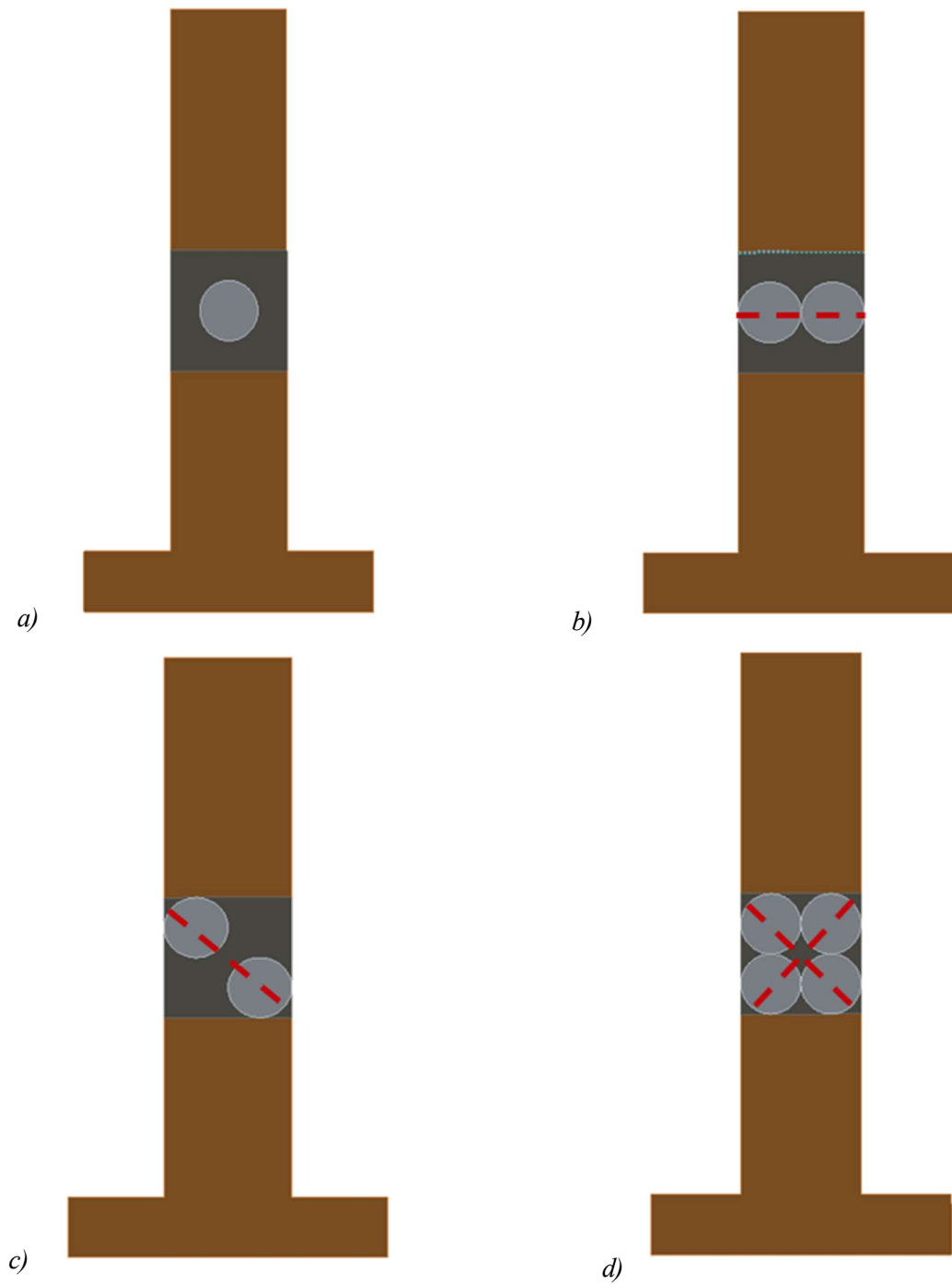


Figure 5-6. Bolt Configurations. a) – single bolt. b) – two bolt horizontal. c) – two bolt diagonal. d)– four bolt.

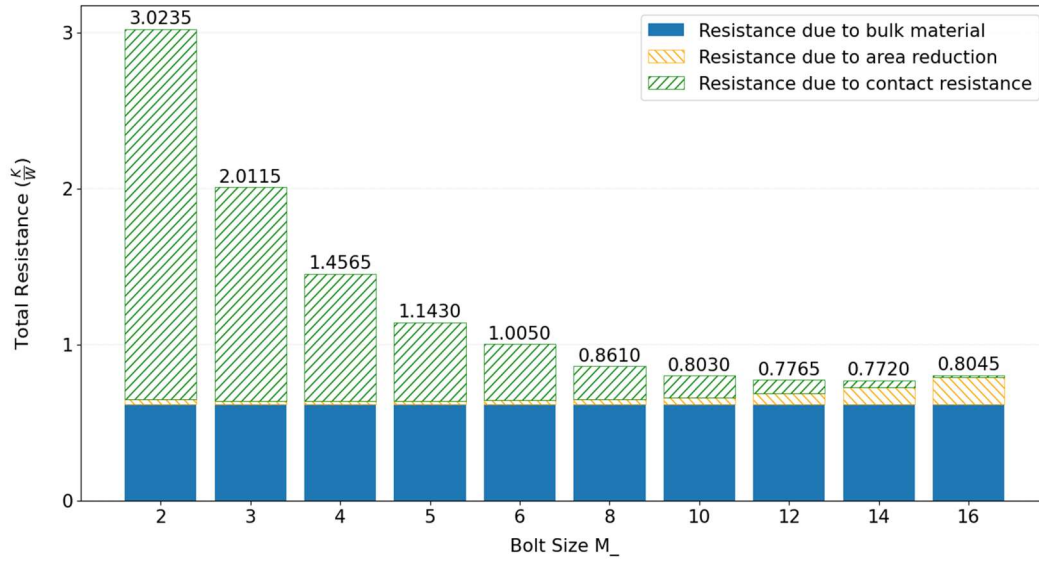


Figure 5-7. Single bolt results.

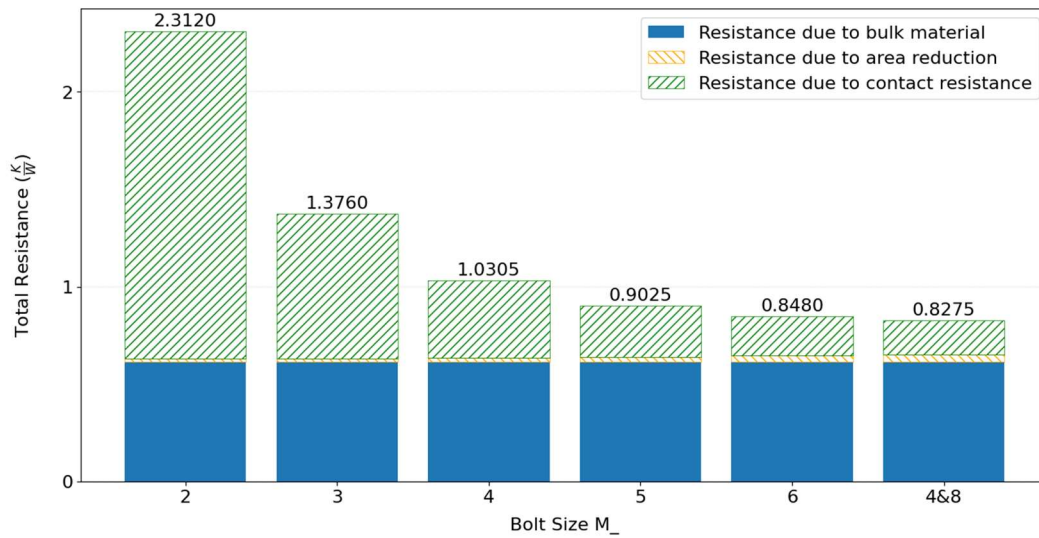


Figure 5-8. Two bolt horizontal results.

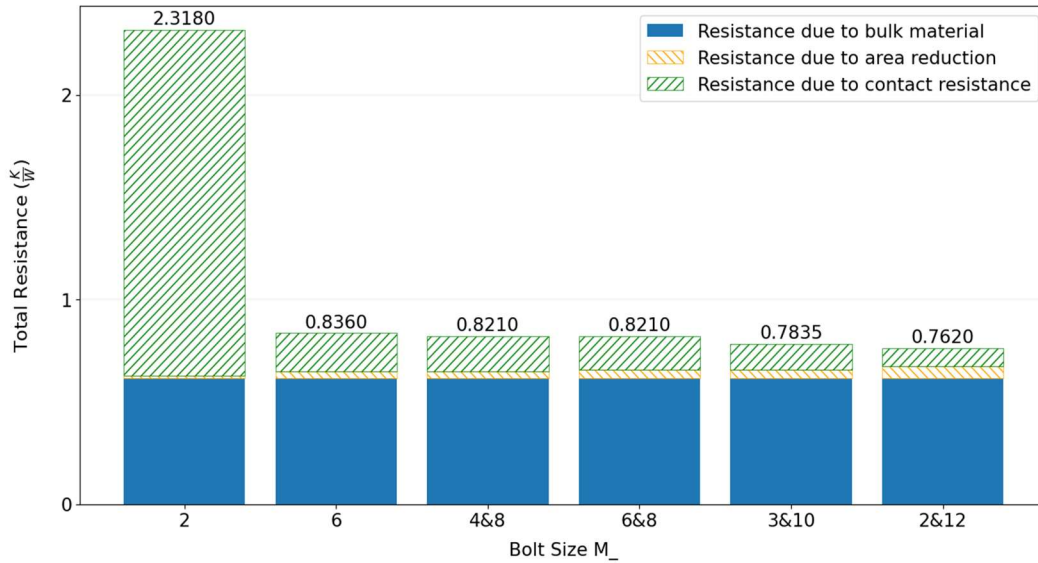


Figure 5-9. Two bolt diagonal results.

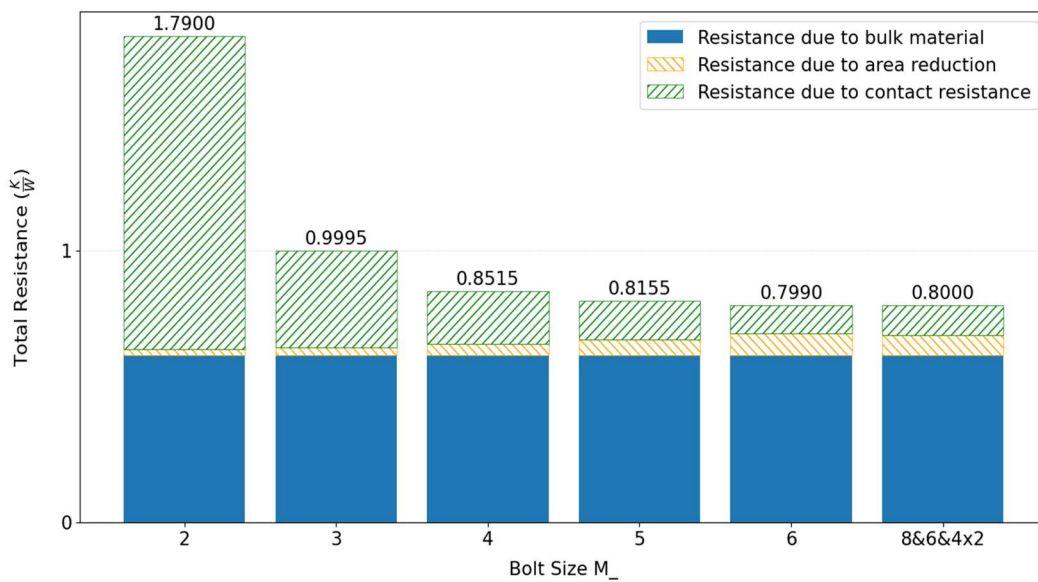


Figure 5-10. Four bolt results.

The data from the various bolt configurations reveals a consistent trend: as bolt sizes increase, the total resistance of the contact decreases. Initially, this decrease occurs rapidly, as thermal contact resistance dominates the total resistance at smaller bolt sizes. However, as bolt sizes increase, the decrease in total

resistance begins to slow down, as the bulk material resistance becomes the dominant resistance component. The similarity of this response suggests a strong correlation between the total resistance and the percentage of the contact interface occupied by bolts. This correlation is depicted in Figure 5-11.

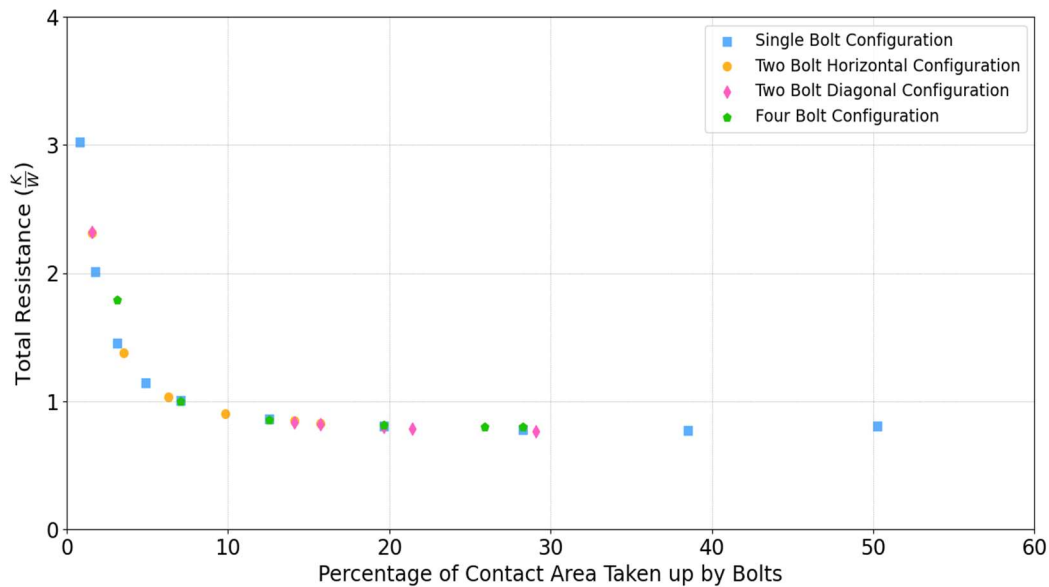


Figure 5-11. Total resistance of the joint as a function of the percentage of the contact area taken up by the bolt.

Figure 5-11 validates this correlation and indicates that there is an optimal range for the percentage of the contact interface occupied by bolts. This optimal range extends from approximately 15% to about 50%. In the present study, data collection ceased when 50% of the contact interface was occupied by bolts. At this point the total resistance has begun to increase due to an increase in the resistance caused by area reduction; this can be seen in the single bolt results shown in Figure 5-7. Configurations past this point are non-optimal both in terms of the value of total resistance and in terms of creating reasonable connections without any bolt head spillover.

Figure 5-11 indicates that the specific bolt configuration utilized to achieve the optimal bolt occupation percentage does not matter. This becomes evident when examining the results where 30% of the contact area was occupied by bolts. Three different bolt configurations, single bolt, two bolt diagonal,

and four-bolt exhibit similar values of total resistance at this bolt coverage. This was also confirmed by the fact that the plotted data from all bolt configurations share the same shape and closely overlap with one another.

5.5 Conclusions

Listed below are the main conclusions that have been drawn from the bolted joint simulation results:

- According to the simulations performed, the main factor to consider when thermally optimizing a bolted joint is the percentage of the contact area that is taken up by bolts. The optimal range for the given contact conditions was found to span from about 15% all the way to 50%.
- It was found that as long as the same percentage of contact area was taken up by the bolts, the total resistance was independent of specific bolt configurations.

6 Conclusion

The work in this report has begun the process of allowing for more informed design decisions to be made on the design of cryogenic systems. A previously constructed test facility was utilized to investigate a number of material properties and then created a simulation framework to obtain a better understanding of a specific component of cryogenic designs.

The two cryogenic material properties investigated were thermal bulk conductivity and thermal contact resistance of OFHC C101 copper. Thermal bulk conductivity tests were performed on samples sourced from three different commercial vendors and it was found that there was variation between sources. The RRR range for all samples in this work was roughly 50 to 80, however if a single value needed to be chosen the results indicate that it should be 75. Thermal contact resistance tests were performed on samples with gold-plated interfaces over a wide range of pressures at the contact interface. Through these tests it was found that increasing the pressure at the interface resulted in the decrease in thermal contact resistance. However, it was found that as pressure increased, the reduction in thermal contact resistance became smaller. Additionally, from these tests, a function was created that allows thermal contact resistance to be determined over a range of temperatures and pressures for the given interface conditions.

The material property information collected was utilized to thermally optimize the design of a common connection type, a bolted joint. This was completed using a simulation framework that was designed to identify the magnitude of the different sources of thermal resistance. The joint was then optimized through the parameterization of the bolt configuration. Through these simulations, it was found that the thermally optimal bolt configuration was strongly related to the percentage of the contact area taken up by the bolts. It was found that a minimization resistance occurred when this percentage was between 10% and at least 50%.

Currently, due to the project being in its preliminary stages, the breadth of the design decisions that can be made from this work is relatively small. For that reason, the main focus of future work should be on

continuing to investigate additional material property data. This will allow for informed thermal designs to be made for a wide range of components or whole systems without the need for physical testing.

7 References

- [1] K. Salmon, "Experimental Characterization of Cryogenic Materials Contact Resistance," Madison, 2021.
- [2] J. W. Ekin, *Experimental Techniques For Low-Temperature Measurements*, Oxford: Oxford University Press, 2006.
- [3] "SHI Cryogenics Group," [Online]. Available: <https://www.shicryogenics.com/product/rdk-415d2-4k-cryocooler-series/>. [Accessed January 2024].
- [4] "Lake Shore Cryotronics," [Online]. Available: https://www.lakeshore.com/docs/default-source/temperature-catalog/lstc_appendixd_1.pdf?sfvrsn=51250de_5. [Accessed January 2024].
- [5] J. Tuttle, E. Canavan and A. Jahromi, "Cryogenic thermal conductivity measurements on candidate materials for space missions," *Cryogenics*, Greenbelt, 2017.
- [6] A. International, "Standard Test Method for Thermal Conductivity of SOLids Using the Guarded-Comparative-Longitudinal Heat Flow Technique," ASTM International, 2020.
- [7] J. W. Ekin, *Experimental Techniques For Low-Temperature Measurements*, Oxford: Oxford University Press, 2006.
- [8] "Lake Shore Cryotronics," [Online]. Available: <https://www.lakeshore.com/>. [Accessed January 2024].
- [9] "Sequoia Brass & Copper," [Online]. Available: <https://www.sequoia-brass-copper.com/>. [Accessed January 2024].

- [10] "McMaster-Carr," [Online]. Available: <https://www.mcmaster.com/>. [Accessed January 2024].
- [11] "thyssenkrupp," [Online]. Available: <https://www.thyssenkrupp.com/en/home>. [Accessed January 2024].
- [12] "Thermal Space," 2016. [Online]. Available: <https://thermal-space.com/thermal-straps/thin-metal-foil-thermal-straps/>. [Accessed January 2024].
- [13] [Online]. Available: <https://trc.nist.gov/cryogenics/materials/materialproperties.htm>.
- [14] J. G. Hust and A. B. Lankford, "Thermal Conductivity of Aluminum, Copper, Iron, And Tungsten For Temperatures From 1 K To The Melting Point," National Bureau of Standards, Boulder, 1984.
- [15] V. A. Yastrebov, *Contact Mechanics and Elements of Tribology*, Evry, 2016.
- [16] A. K. J. Hasselstrom and U. E. Nilsson, "Thermal Contact Conductance in Bolted Joints," Chalmers University of Technology, Gothenburg, 2012.
- [17] V. Andersson, "Thermal Contact Conductance in Aircraft Applications," Lulea University of Technology, Lulea, 2018.
- [18] J. A. Greenwood and J. B. P. Williamson, "Contact of nominally flat surfaces," The Royal Society, London, 1966.
- [19] M. R. Mahadeshwara, "Tribonet," 10 November 2022. [Online]. Available: <https://www.tribonet.org/wiki/greenwood-williamson-model/>. [Accessed January 2024].
- [20] K. A. Woodbury, H. Najafi, F. d. Monte and J. V. Beck, "Inverse Heat Conduction Problems: An Overview," in *Inverse Heat Conduction: III-Posed Problems*, John Wiley & Sons, Inc., 2023, pp. 1-23.

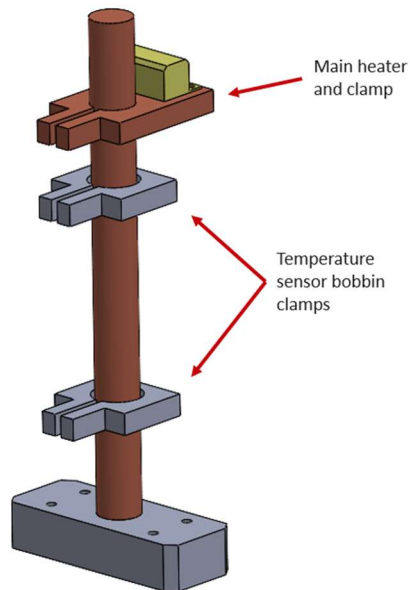
- [21] B. Sponagle and D. Groulx, "Measurement of thermal interface conductance at variable clamping pressures using a steady state method," *Applied Thermal Engineering*, vol. 96, pp. 671-681, 2015.
- [22] A. Tariq and M. Asif, "Experimental investigation of thermal contact conductance for nominally flat metallic contact," *Heat and Mass Transfer*, vol. 52, pp. 291-307, 2015.
- [23] A. Dillon, K. McCusker, J. V. Dyke, B. Isler and M. Christiansen, "Thermal interface material characterization for cryogenic electronic packaging solutions," in *IOP Conference Series: Materials Science and Engineering*, Gothenburg, 2017.
- [24] H. M. Ledbetter, "Temperature behavior of Young's moduli of forty engineering alloys," *Cryogenics*, vol. 22, no. 12, pp. 653-656, 1982.
- [25] W. M. Rohsenow, *Handbook of Heat Transfer*, New York: McGraw-Hill, 1998.
- [26] I. Fernlund, *A method to calculate the pressure between bolted or riveted plates*, Göteborg: Chalmers University Books, 1961.
- [27] R. G. Budynas and J. K. Nisbett, *Mechanical Engineering Design*, McGraw Hill, 2024.

Appendix A: Thermal Bulk Conductivity Procedure & Data Processing

Test Procedure

Sample Preparation

Samples used in the bulk conductivity tests consist of 6-inch long, $\frac{1}{2}$ inch diameter rods. The process for mounting these samples is described below.



1. Mount the knife-edge clamps onto the rod. Then bolt the temperature sensors to the knife-edge clamps with T2 mounted near the base of the rod and T1 mounted near the floating end of the rod. The base of the rod is distinguished by a threaded hole that is used to connect it to the aluminum base.
2. Record five measurements of both the diameter of the rod and the length between the temperature sensor location. Keep in mind that this length measurement should be between the top surfaces of both knife edge clamps. Insert these measurements into the 'measurement' excel sheet.
3. Mount the heater clamp, with the heater attached, to the top of the rod. Ensure the heater leads are connected to the power supply and the multimeter, two sets of two wire leads (one set going to each device). This connection can be verified by testing the heater and measurement function in the LabView code. If the code reads no current, the circuit is open which indicates there is a disconnect

somewhere, check connection points and solder locations. If the code reads negative power, one of the two sets of wire leads needs to be reversed.

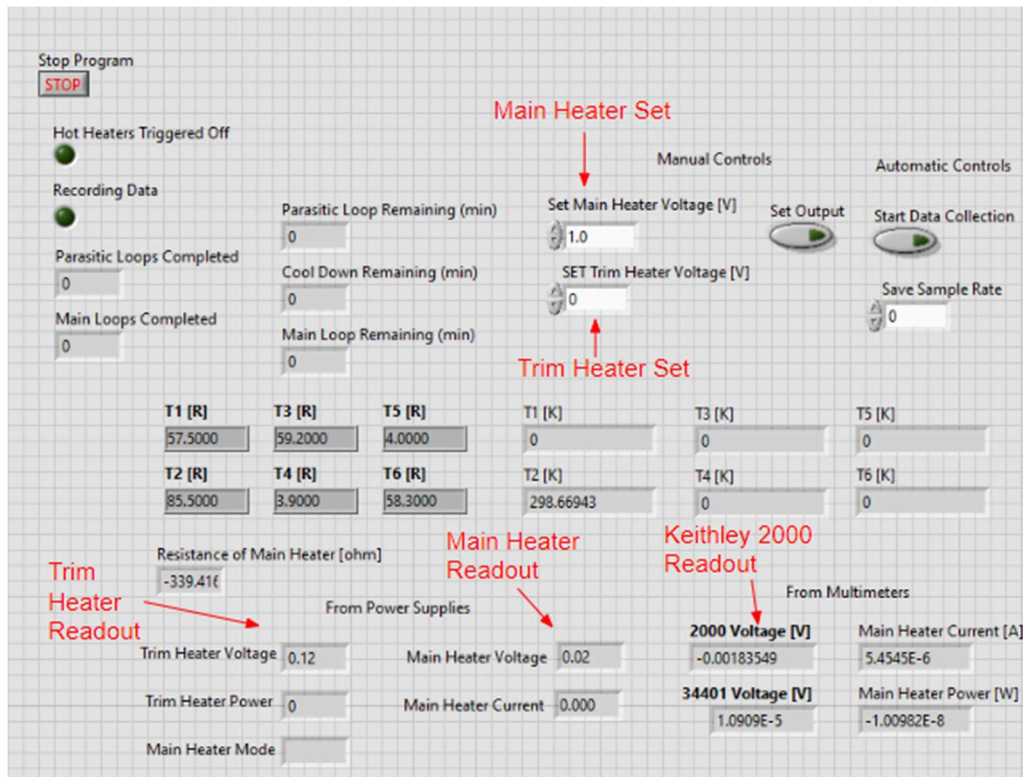
4. Mount the copper rod into the aluminum sample base with a #4-40 bolt ensuring a tight secure connection. Apiezon grease should be spread at the contact interface between the rod and aluminum base, in a layer about as thick as the surface roughness at the interface.
5. Mount the aluminum base onto the sample stage with four #4-40 bolts. Again, ensure Apiezon grease is spread at the contact interface between the sample stage and the aluminum base.

Sensor Check

Once the sample is successfully mounted onto the second stage cold plate, ensure the temperature sensors and heaters (trim and main) are all functioning and recording data correctly with the LabView main code.

1. Ensure all instrumentation is on, specifically the BK Precision 1685B, BK Precision 1698, HP 34401A, Keithley 2000, and Lakeshore 218.
2. A majority of the temperature sensors are not calibrated up to room temperature, so a reading of 0 in the code is normal. To ensure that the temperature sensors are functioning properly, make sure the resistance reading on the sensor is stabilized and reading between 0 and 100. Any large positive, negative, or fluctuating reading indicates a malfunctioning sensor; if this is the case check connection points for any open circuits.
3. Ensure the heaters are both connected. The main heater requires a four-wire connection, one two-wire set connects to the BK 1698 power supply and the other two-wire set connects to the Keithley 2000 multimeter. The trim heater requires a two-wire connection and is connected to the BK 1685B power supply. To test the heaters are functioning properly run the following tests:
 - a. In the LabVIEW code, set the trim heater to 5V. Ensure that the power supply readout matches the voltage set and that the trim heater power reads a non-zero value. Set the trim heater back to 0V. (See figure below)

- b. In the LabVIEW code, set the main heater to 5V (will need to click the “set output” button to close the circuit). Ensure that the power supply and Keithley 2000 multimeter readouts match the voltage set. The remaining multimeter measurements should also read non-zero values. Set the main heater back to 0V. (See figure below)



System Closing and Preparation

After mounting the sample and checking sensors, close the system to begin testing. This consists of first closing the thermal jackets and then the vacuum chamber itself. While doing this, **do not place tools on the vacuum chamber edge and always wear gloves when handling MLI.**

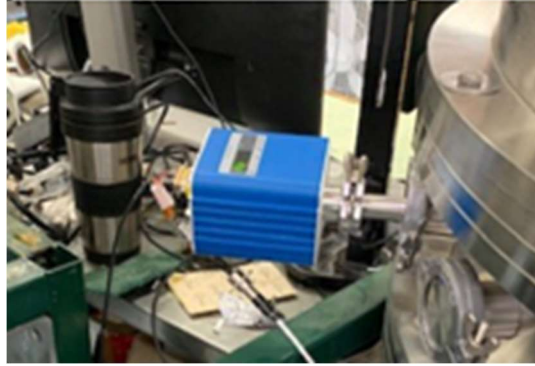
1. Carefully place the second stage thermal jacket onto the sample stage and tightly bolt the jacket into place (6 bolts).
2. Velcro the top portion of the MLI to the bottom portion (4 straps).



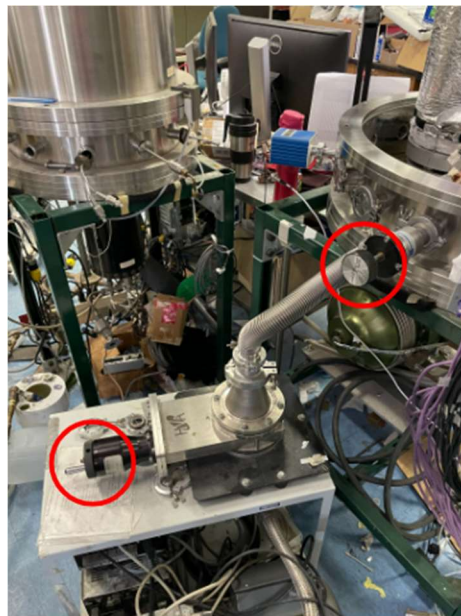
3. Place the bottom flange and outer jacket (the larger MLI covered aluminum can) carefully onto the first stage. **Ensure no wires are pinched or disconnected in this process and perform a second sensor check after placing the jacket down.** Tightly bolt the jacket and flange into place (8 bolts) and attach the extra strips of MLI around the flange.
4. Attach the bottom MLI to the MLI around the outer jacket with the 2 velcro strips. **Ensure no MLI sheets from the jacket are touching the vacuum chamber walls.**
5. Using a Kimwipe and isopropyl alcohol, clean the inside and edge of the vacuum chamber.
6. **Before closing the vacuum chamber, ensure no tools are left within the vacuum chamber.**
7. Lower the bell jar of the vacuum chamber slowly with one hand supporting it as it is lowered. Make sure to not touch the chamber O-ring.
8. Fasten the six bolts on the vacuum chamber in a star pattern and then in a circle, a similar process to bolting a tire, to ensure even bolting.

Starting Vacuum

1. Ensure the vacuum gage (Grainville Phillips Micro-Ion Plus) is turned on and powered. It is powered with a wall plug adaptor.



2. Secure the vacuum hose attached to the vacuum cart to the chamber valve. The KF-flange fitting is connected with an O-ring between the hose and the fitting on the chamber. Tighten the clamp around the connected fittings by hand.
3. Ensure that the pump valve and chamber valve are both opened. These two valve knobs are circled below in red.



4. With the vacuum pump plugged into its wall power supply, flip the switch labeled 'convertor' to the on position to turn on the electronics of the vacuum pump.
5. Flip on the 'vane pump' switch to turn on the roughing pump.

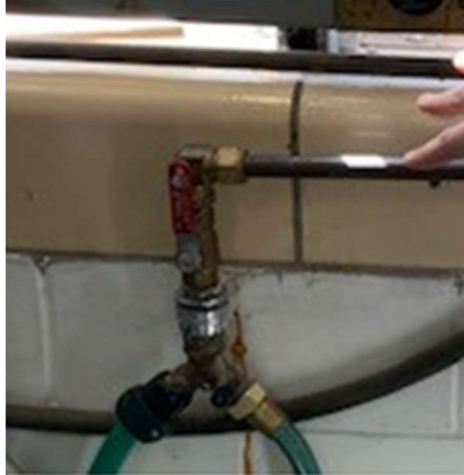
6. Monitor the chamber pressure either on the Grainville Phillips Micro-Ion Plus gage itself or using the LabVIEW code 'vacuum gauge readout', wait until the chamber pressure is below 0.1 Torr before turning on the turbo pump.
7. Before turning on the turbo pump, check the vacuum chamber bolts and tighten if needed.
8. Press the 'start' button on the vacuum cart below the convertor and vane pump switches to turn on the turbo pump.
9. After the turbo pump is on and the chamber pressure is below 0.02 Torr, the cryocooler can be turned on.

Starting the Cryocooler

1. Turn on the power supply to the pump running the distilled water that cools the compressor. The pump runs at a max voltage of 10 V, but for our purposes run the pump between 9-10 V.



2. Check that the distilled water reservoir is sufficiently filled. The reservoir is the tubing located above the T-joint in the image above. There should always be water above the T-joint while the system is running.
3. Turn on the facility water to the heat exchanger by opening the red valve. In the image the valve is in the open position, if turned parallel to the ground the valve is in the closed position. The facility water is used to remove heat from the distilled water loop inside the heat exchanger.



4. Turn the main power switch of the compressor to 'on'. This is vertical as shown in the picture circled in red.



5. Press the 'On' button on the compressor to start running. This is shown in the picture below circled in red.



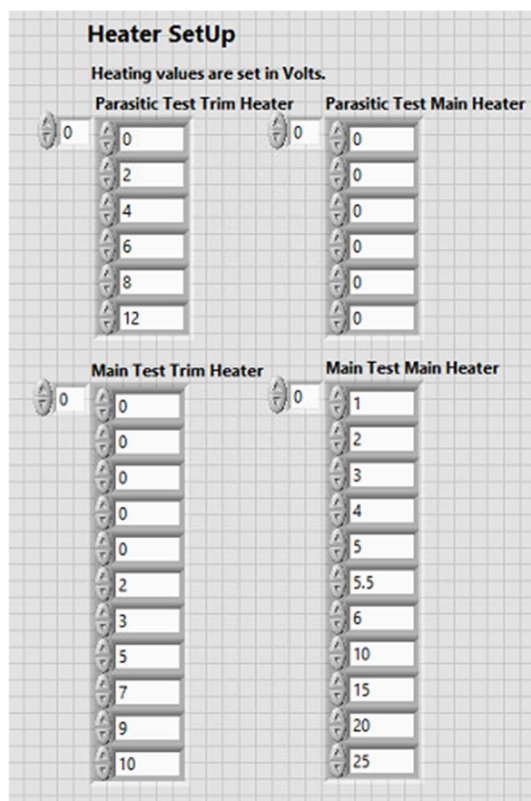
Data Collection

1. Once the experiment has reached a cold steady state, testing can begin. This can be determined when the temperature of all sensors is no longer changing.
2. Create a heating power test matrix for each thermal bulk conductivity test (can be kept the same if the sample material is the same). As the experimentalist, you can decide what temperature range you are interested in testing and how many data points you want to collect.
 - a. Parasitic Heating Values: Use the trim heater (and trim heater only) to vary the temperature of the sample over the temperature range of interest. Record an N number of heater set points that cover that range.
 - b. Main Heating Values: Use a combination of the main heater and trim heater to vary the temperature of the sample over the temperature range of interest. Record an N number of heater set points that cover that range. When recording the heater values, the temperature difference between the two sensors must be large enough to be outside of their measurement uncertainty while still being close enough to ensure the conductivity value measured corresponds to the correct temperature; the main heater changes this temperature difference while the trim heater changes the overall temperature of the system.

Heating Power Test Matrix Example for Thermal Bulk Conductivity			
Data	Trim Heater Voltage (V)	Main Heater Voltage (V)	Goal Temperature (K)
	0	0	

Parasitic	2	0	
	4	0	
	6	0	
	8	0	
	12	0	
Main	0	1	4
	0	2	5
	0	3	6
	0	4	7
	0	5	8
	2	5.5	9
	3	6	10
	5	10	15
	7	15	20
	9	20	30
10	25	40	

3. Insert the heating power test matrix into the automated LabVIEW array elements as shown in the images below. These array elements are located in the front panel of the LabVIEW code under the section labeled 'Automated Test Setup'.



4. Set timer elements to a long enough time period to allow for the system to reach a steady state between heating increments. A test matrix for C101 samples is shown in the table below; if using a different material these times may need to be changed. These timer array elements are located in the front panel of the LabVIEW code under the section labeled ‘Automated Test SetUp’.

Wait Timer Values for C101 Samples		
Heater Timers	Heater Wait Timer	15 min (900,000 ms)
	Heater Cooldown Timer	30 min (1,800,000 ms)
Data Collection Timers	Data Collection Wait Timer	14 min (840,000 ms)
	Data Collection Timer	1 min (60,000 ms)
	Data Collection Cooldown Timer	30 min (1,800,000 ms)

Timer SetUp

Heater wait timers must be equal to the combination of the data collection wait timer and the data collection timer. Timers are set in milliseconds.

Parasitic Test Heater Wait Timer	900000	Parasitic Test Data Collection Wait Timer	840000
		Parasitic Test Data Collection Timer	60000
Heater Cooldown Timer	1800000	Data Collection Cooldown Timer	1800000
Main Test Heater Wait Timer	900000	Main Test Data Collection Wait Timer	840000
		Main Test Data Collection Timer	60000

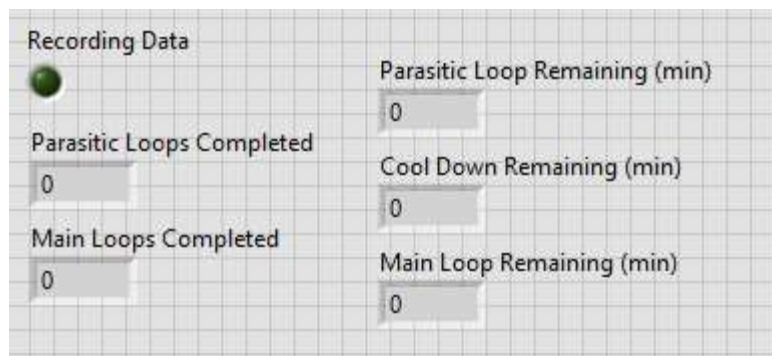
- Fill in file path array elements in the LabVIEW code. This is the location the TDMS file containing the data for the specific data point will be sent. These array elements are located in the front panel of the LabVIEW code under the section labeled 'Automated Test SetUp'. Ensure that each file path is unique.

File Path SetUp

Number of file paths must be equivalent to the number of heater values set. Each file path must be unique.

Parasitic Data File Paths	Main Data File Paths
0	0
C:\Users\jvalois\Documents\FCHFLast1\p1	C:\Users\jvalois\Documents\FCHFLast1\m1
C:\Users\jvalois\Documents\FCHFLast1\p2	C:\Users\jvalois\Documents\FCHFLast1\m2
C:\Users\jvalois\Documents\FCHFLast1\p3	C:\Users\jvalois\Documents\FCHFLast1\m3
C:\Users\jvalois\Documents\FCHFLast1\p4	C:\Users\jvalois\Documents\FCHFLast1\m4
C:\Users\jvalois\Documents\FCHFLast1\p5	C:\Users\jvalois\Documents\FCHFLast1\m5
C:\Users\jvalois\Documents\FCHFLast1\p6	C:\Users\jvalois\Documents\FCHFLast1\m6
	C:\Users\jvalois\Documents\FCHFLast1\m7
	C:\Users\jvalois\Documents\FCHFLast1\m8
	C:\Users\jvalois\Documents\FCHFLast1\m9
	C:\Users\jvalois\Documents\FCHFLast1\m10

- On the LabVIEW front panel click the 'Start Data Collection' button. The code will now run automatically until all data points have been collected. On the front panel are loop counts and loop timers which allow the user to monitor the progress of the data collection.



Cryocooler Off and Returning to Room Temperature

- Press the 'off' button on the compressor to the left of the 'on' button.
- Turn the main power switch on the compressor to the off position.
- Turn the facility water red valve to the closed position.
- Turn off the water pump power supply.
- Set the main heater to 25 V and the trim heater to 37 V to heat the experiment to room temperature, this generally takes half a day to equilibrate. Ensure to not heat the chamber to temperatures higher than room temperature.

Stopping Vacuum and Opening the Chamber

- Remove all of the bolts on the vacuum chamber.
- Close both the turbo pump and chamber valves.
- Undo the clamp that connects the hose to the chamber valve to separate the vacuum cart from the chamber.
- Stop the turbo pump by pushing the 'stop' button.
- Stop the roughing pump by switching the vane pump switch to off.
- Turn off the electronics by switching the converter switch to off.

7. **Slowly vent the turbo pump by opening the valve until you hear the spinning change (gets slightly louder), then stop adjusting the valve and wait for the turbo to spin down and the sound to stop.**
8. **Once the spinning stops, open the valve all the way to fully expose the turbo pump to room pressure.**
9. Open the vacuum chamber valve slowly to vent the chamber to room pressure as well.
10. Slowly lift the vacuum chamber bell jar open to access the chamber inside.
11. **Put gloves on and take apart the MLI and thermal jackets to access the sample within.**
12. Once the jackets are off, disassemble the sample fixture to prepare for the next test.

Data Processing and Calculation

The data from LabVIEW is stored in TDMS files under the file names that were set in the LabVIEW array elements. Opening these TDMS files, all of the data for each point can be extracted. Copy 200 rows from the TDMS file and paste them into the appropriate excel files (either parasitic or main). Then run the Thermal Bulk Conductivity Python code to obtain the results from the post processing calculations.

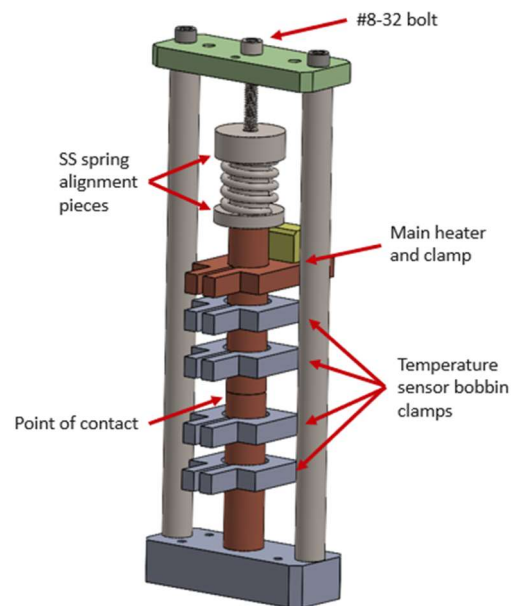
Appendix B: Thermal Contact Resistance Procedure & Data Processing

Test Procedure

Sample Preparation

Samples for the thermal contact resistance testing consist of two 2.25-inch long, $\frac{1}{2}$ inch diameter rods.

Mounting these samples in the test fixture is described below.



1. Mount the knife-edge clamps with the attached temperature sensors onto the rods. The sensors are mounted in the order shown above. When mounting the clamps, ensure they are inserted over the non-contact edge so that the contact is not damaged.
2. Record 5 measurements each for the following measurements: diameter of the top sample, diameter of the bottom sample, length between T6 and T2, length between T2 and contact interface, length between contact interface and T1, and length between T1 and T5. Insert these measurements into the 'measurement' excel sheet.
3. Mount the heater clamp to the top end of the upper rod. Ensure the heater is mounted far enough from the top end to allow the spring holder to be mounted.

4. If applicable to the test, clean the contact interface with isopropyl alcohol and Kim wipes. Then, record a pressure paper measurement. Remove the pressure paper and re-clean the interface.
5. If applicable apply a TIM.
6. Re-mount the samples within the spring assembly and tighten to the desired pressure using the #8-32 bolt at the top of the fixture.
7. Mount the aluminum base to the sample stage with four #4-40 bolts. Ensure Apiezon Grease is in place between the contact of the sample stage and aluminum base.

Sensor Check

*Follow the Thermal Bulk Conductivity Test Procedure - **Sensor Check**

System Closing and Preparation

*Follow the Thermal Bulk Conductivity Test Procedure - **System Closing and Preparation**

Starting Vacuum

*Follow the Thermal Bulk Conductivity Test Procedure - **Starting Vacuum**

Starting the Cryocooler

*Follow the Thermal Bulk Conductivity Test Procedure - **Starting the Cryocooler**

Data Collection

*Follow the Thermal Bulk Conductivity Test Procedure - **Data Collection**

Note that the heating values and timer values will need to be altered as the test and fixture are different. For the heater values, ensure there are an adequate number of values selected that span the temperature range of interest; follow the method described in the thermal bulk conductivity test procedure for setting these values. For the timer values, because of the additional components of the fixture, it will take longer to reach a steady state between data points. To find the appropriate timer times, record the amount of time it takes to reach a steady state after increasing the heat applied; add an additional buffer time to ensure that steady state is reached.

Cryocooler Off and Returning to Room Temperature

*Follow the Thermal Bulk Conductivity Test Procedure - **Cryocooler Off and Returning to Room Temperature**

Stopping Vacuum and Opening the Chamber

*Follow the Thermal Bulk Conductivity Test Procedure - Stopping Vacuum and Opening the Chamber

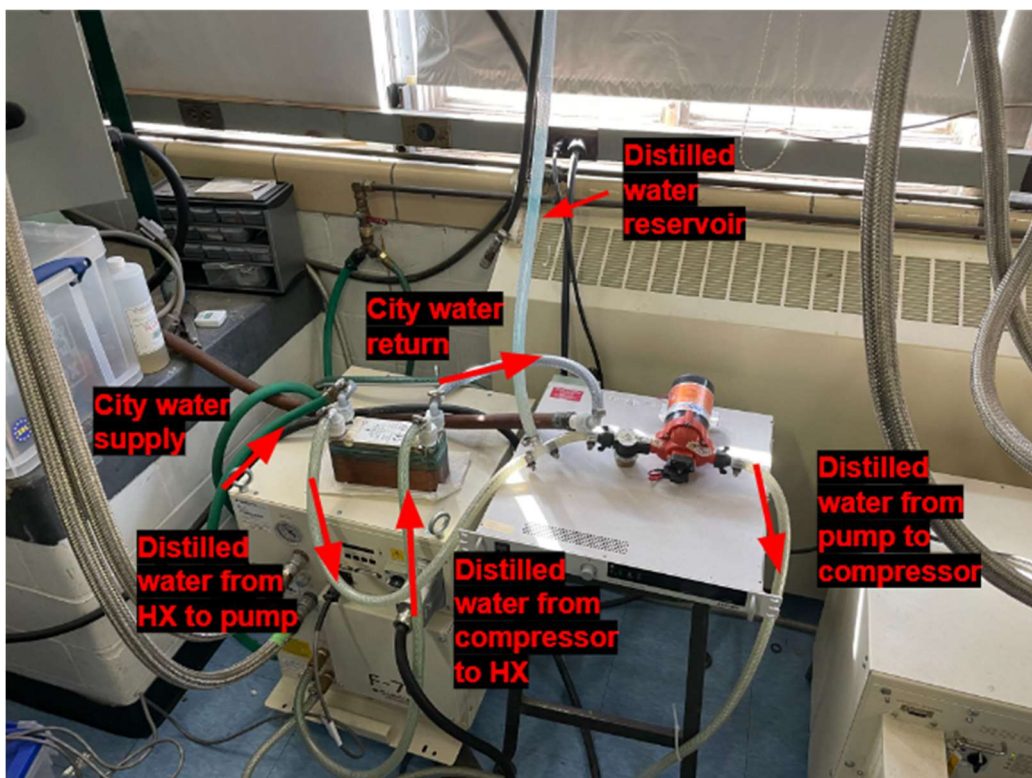
Data Processing and Calculation

The data from LabVIEW is stored in TDMS files under the file names that were set in the LabVIEW array elements. Opening these TDMS files, all of the data for each point can be extracted. Copy 200 rows from the TDMS file and paste them into the appropriate excel files (either parasitic or main). Then run the Thermal Contact Resistance Python code to obtain the results from the post processing calculations.

Appendix C: Test Facility 'Wiring' Diagrams

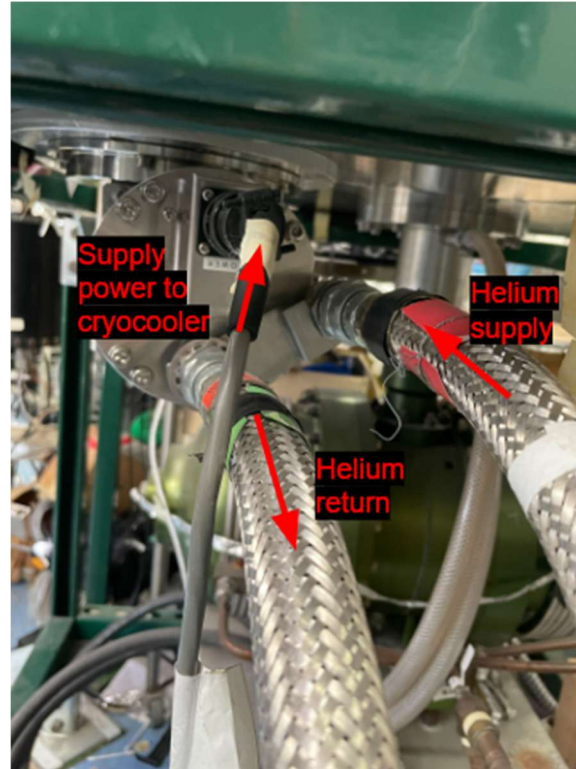
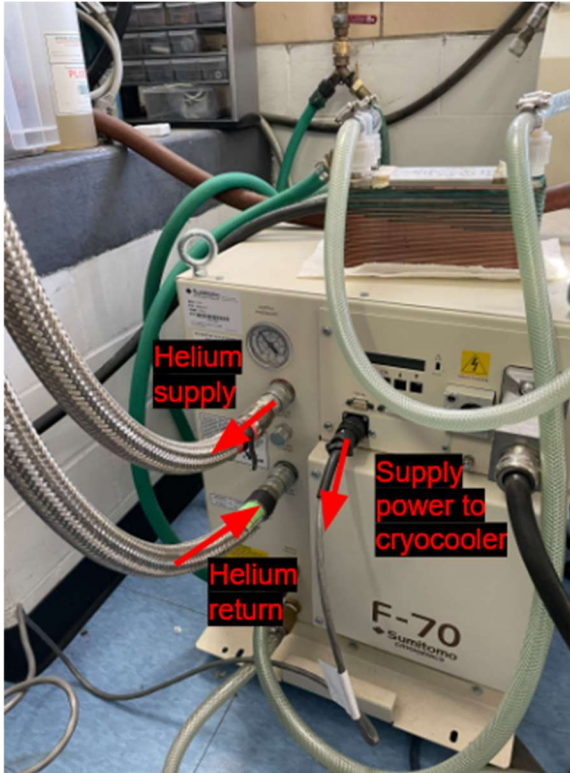
Compressor Cooling Loop

The compressor is cooled using distilled water. In order to not need to have a significantly large reservoir of distilled water, a closed loop supply system is used. The distilled water in the closed loop is circulated using a SEAFLO SFDP1-030-045-33 water pump to provide the compressor with enough coolant, at least 1.6 GPM, during operation. The distilled water releases heat to cool city water in an external heat exchanger. The figure below outlines components of this compressor cooling loop.



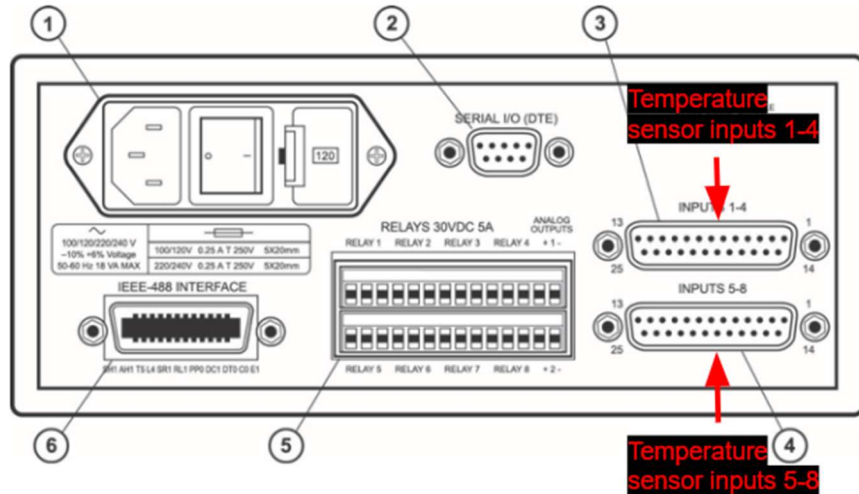
Helium Supply Loop

The compressor provides high pressure Helium and power to the cryocooler mounted inside the bell jar. The cryocooler then returns low pressure helium to the compressor. The Figure below shows the Helium supply loop. To see how the Liquid Helium Dampening Pot interacts with this loop reference Figure 2-6.



Temperature Sensor Wiring Loop

Temperature sensor wiring runs from the Lake Shore 218 Temperature monitor located on the equipment cart to the temperature sensors located at the second stage of the cold head. The connection points for the 8 temperature sensors on the Lake Shore 218 temperature sensors can be seen in the figures below.



Input Connector (Inputs 1-4)				Input Connector (Inputs 5-8)			
PIN	DESC.	PIN	DESC.	PIN	DESC.	PIN	DESC.
1	NC			1	NC		
2	S	14	S	2	S	14	S
3	1I+	15	1I-	3	5I+	15	5I-
4	1V+	16	1V-	4	5V+	16	5V-
5	S	17	S	5	S	17	S
6	2I+	18	2I-	6	6I+	18	6I-
7	2V+	19	2V-	7	6V+	19	6V-
8	S	20	S	8	S	20	S
9	3I+	21	3I-	9	7I+	21	7I-
10	3V+	22	3V-	10	7V+	22	7V-
11	S	23	S	11	S	23	S
12	4I+	24	4I-	12	8I+	24	8I-
13	4V+	25	4V-	13	8V+	25	8V-

The wiring colors that correspond to the I+, I-, V+, and V- can be seen in the table below. These colors apply to the wiring from the temperature monitor to the temperature sensors itself.

I+	White
V+	Red
I-	Black
V-	Green

Temperature sensor wiring is fed into the bell jar through an external box. The wiring (black cabling) enters through the top of the box and are fed into the bell jar through an opening that is located around the circumference of the bell jar. Within the bell jar, the wiring is fed through the base plate of both cold stages to its final location at the second stage. At both the first stage and the second stage, the temperature sensors are labeled corresponding to their sensor position in the LabVIEW code. Engraved on each temperature sensor is its unique identifying sensor numbering.

Heater Wiring Loops

Trim Heater Wiring

The trim heater is powered by the BK Precision 1685B DC Power Supply. From the power supply, the positive terminal is attached to the red wire and the negative terminal is connected to the green wire. All heater wire that connects the external instrumentation and the connection point to enter the bell jar is located within the white cabling. The heating wire for the trim heater enters the heater feedthrough box using the 3rd slot. Within the bell jar, at the first stage cold head there is a connection point used to extend the length of the cabling to reach the second stage. The connection is performed using the top two terminals and the wiring for both ends of the connection is labeled “Trim”. At the second stage cold head, the heater wire terminates at the trim heater mounted on the cold plate.

Main Heater Wiring

The main heater is powered by the BK Precision 1698 DC Power Supply. The black wire is connected to the positive terminal of the power supply; this wire runs all the way to the main heater. The red and green wires are connected to the positive and negative terminals of the Keithley 2000 Multimeter respectively. These wires also run to the main heater and record the voltage across the resistive heater. The white wire is the return wire from the main heater. This return is connected to one end of the shunt resistor, while the other end of the shunt resistor is connected to the negative terminal of the power supply. The HP 34401A multimeter is connected to the middle two terminals of the shunt resistor and measures the voltage that is eventually converted into current.

It is important to note that wire extenders were used of various colors, the colors referred to in the previous paragraph correspond to the wire colors leaving the white cabling

All heater wire that connects the external instrumentation to the connection point to enter the bell jar is located within the white cabling. The heating wire for the main heater enters the heater feedthrough box using the 1st slot. Within the bell jar, at the first stage cold head there is a connection point used to extend the length of the cabling to reach the second stage. The bottom two terminals of this connection are where the power supply leads are connected (black and white). The top two terminals of this connection are where the multimeter leads are connected (red and green). Both sides of this connection are labeled as “Main”. If any of the values are reported as negative, the two wires for that connection need to be flipped. At the second stage cold head, the heater wire terminates at the main heater mounted on the copper clamp.